Synthesis, Fabrication, and Characterization of Nanostructures from Spent Reforming Catalysts

By

Muhammad Awais Khan

School of Chemical and Materials Engineering

National University of Sciences and Technology

2021

Synthesis, Fabrication, and Characterization of Nanostructures from Spent Reforming Catalysts

Names: Muhammad Awais Khan

Reg.No: 275710

This thesis is submitted as a partial fulfillment of the requirements for the degree of

MS in Chemical Engineering

Supervisor Name: Dr. Muhammad Taqi Mehran

School of Chemical and Materials Engineering (SCME)

National University of Sciences and Technology (NUST)

H-12 Islamabad, Pakistan

February 2021

Dedication

This thesis is dedicated to my beloved father, mother, siblings, nieces, nephews, friends, teachers, and all the beautiful people who seek(s) knowledge, truth, wisdom, and love.

Acknowledgments

First and foremost, I am grateful to Almighty Allah, the creator of living souls. I am in a debt of gratitude to my respected supervisor, Dr. Muhammed Taqi Mehran, for believing in my abilities. His incessant direction, encouragement and support was the driving force behind the success of this project. I would encompass my sincere thankfulness to my worthy GEC members, **Dr. Salman Raza Naqvi, Dr Umair Sikander** and **Dr. Aftab Akram** who supported me in my lab work and technicalities of my research. The words are not enough to compliment my loving and sweet mother who has been my intellectual and spiritual inspiration for me. Her never-ending efforts and prayers sustained me at every stage of my life and invigorated me for attaining high goals. The greatest credit goes to my father who supported me on every part of this journey. I can never payback the encouragement, affection, and money of my father, who stimulated me to pursue my dream and complete my MS study. Lastly, I would love to pay my special thanks to my siblings, thank you very much for understanding the load of this journey and supporting me morally.

Abstract

It is extremely prudent and highly challenging to design an economical bifunctional electrocatalyst with effective electrocatalytic activity and high stability catalyst for electrochemical water splitting. As hundred tons of catalyst is annually deactivated by coking, so herein, we came up with a strategy to utilize spent methane reforming catalysts that were deactivated by formation of graphitic and fibrous carbon. An electrocatalyst of noble-metal free MoS_2 and spent catalysts was successfully synthesized using cost effective and environmentally friendly hydrothermal method, which showed an exceptional performance towards hydrogen evolution reaction (HER) as well as oxygen evolution reaction (OER). At 25 mA cm^{-2} a phenomenal OER overpotential (η_{25}) of 128 mV and 154 mV, while a modest HER η_{25} of 186 mV and 207 mV for respectively was resulted for MoS_2@CNF and MoS_2@GC, respectively. Furthermore, the synthesized catalysts exhibited a good long-term durability for about 18 hrs. at 100 μA cm^{-2} with unnoticeable change in HER LSV curve after 1000 cycles. This work of synthesizing an enhanced electrocatalyst from spent catalysts (highly conductive due to carbon) with minimal usage of an expensive MoS_2 (having good electrocatalytic activity) gives a rationale to utilize coked catalysts for obtaining an enhanced electrocatalyst for overall water splitting.

Keywords: *spent methane reforming catalyst, noble-metal free molybdenum sulphides, electrocatalyst, hydrogen evolution reaction, oxygen evolution reaction.*

Table of Contents

List of Figures

List of Tables

List of Abbreviations

OER: Oxygen evolution reaction

HER: Hydrogen evolution reaction

Ni: Nickle

Mn: Manganese

Al: Aluminum

LDH: Layered double hydrotalcite

Mo: Molybdenum

S: Sulphur

CNF: Carbon Nano Fiber

GC: Graphitic Carbon

Oxidation: Ox

Reduction: Red

Manganese: Mn

Pt: Platinum

Chapter No. 1

Introduction

1.1 Discovery of Hydrogen

In 1671, Robert Boyle, while doing experimentation with iron and sulphuric acid, produced a gas which he called as “inflammable solution of iron” [1]. After about a century later while experimenting with mercury, Henry Cavendish produced the same gas and identified it as a distinct element [2]. He thought that instead from acid the gas was released from the metal due to which he called it “inflammable air from metals”. Finally, Antoine Lavoisier recognized its nature and called that gas “hydrogen” (means water forming) [3]. The journey of hydrogen that started almost $3\frac{1}{2}$ century later, is now in the phase where it is pacing up to lead the global race of energy requirement, with an increasing current demand of 70 Mt of H_2/year [4]. Hydrogen is the most abundant gas in the universe that possesses the highest energy content when compared to traditional fuels (3 times energy content of that of gasoline.). The supply of hydrogen from the sun is enough for sustaining hydrogen fusion reaction for about another 5 billion years [5].

1.2 Hydrogen Production

Despite its abundancy, it is difficult to obtain hydrogen in its elemental form different sources. Different conventional sources like fossil fuels, biomass and renewable sources like solar wind, wave etc. are being used for the production of hydrogen. The most common method for generating hydrogen is methane reforming through steam which contribute to about 50% of hydrogen demand while naphtha/oil reforming with 30%, coal gasification with about 18% , water electrolysis with about 3.9% and other resources with 0.1% are currently fulfilling the hydrogen demand [6].

Annually there is about 2.3% rise in the consumption of energy which leads to worrisome increase in CO emission level impacting the environment in the most adverse way. The intergovernmental panel on climate change (IPCC) recently reported an about 1.5 °C increase in the overall temperature of the earth due to greenhouse gas

emissions. The emissions regarding industrial CO_2, are projected to be lowered by 90% in 2050 as compared to 2010. Diverting our dependency from fossil fuels towards green and sustainable fuels like hydrogen through a green, cost effective and sustainable process is the need of hour [7].

1.2.1 Production of Hydrogen from steam reforming

The major contributor of Hydrogen is fossil fuel. Fossil fuels like methanol, ethanol, gasoline, methane and other hydrocarbons are the main source of Hydrogen production [8]. Steam reforming uses natural gas, methanol, and lighter hydrocarbons as its raw material. In the steam reforming process, synthesis gas is produced from steam and the raw materials [9]. This synthesis gas or syn gas consists of carbon monoxide and hydrogen of which the carbon monoxide is converted to carbon dioxide [10]. The temperature which is obtained by combusting raw material with air or oxygen is in the range of about 500 ^oC [11].

The catalysts used in steam reforming can be divided in two main categories i.e. noble metal platinum or rhodium based catalyst and non-precious metal like Nickle based catalyst [12]. As the heat and mass transfer limitations are mainly in action and comparatively the kinetics of the process is not an important factor therefore, the use of Nickle as a catalyst is always industrially preferred [13].

In steam reforming, a significant factor is the atomic ratio of Hydrogen and Carbon (H:C) comprising the feedstock material. As this ratio gets lower the production of Carbon dioxide increases [14]. This production of carbon dioxide is hazardous not only for the environment but also leads to entrapment of sunlight in the earth's atmosphere which leads to global warming [15].

Currently, hydrogen is obtained from synthesis gas (comprising of H_2 and CO) which is obtained through gasification and methane reforming [16]. These processes are emission intensive with 7 kg of CO_2 and 18-20 kg of CO_2 produced per kg of H_2 by methane reforming and gasification, respectively [15,17]. Besides, contributing to greenhouse gases and global warming these processes end in wasting a large amount of catalyst due to coking [18].

1.2.1.1 Coking of electrocatalyst from methane reforming

Coking is a ubiquitous problem for modern petrochemical and energy transformation processes which leads to deactivation of catalyst. In 2009, it was reported that about

150000-170000 tons of catalyst was spent annually, with about 5% of annual increase, it is predicted to be now in the range of 232,500-263,500 t/year [19,20] .Previously, spent catalysts have been utilized by different methods for different purposes but mostly, they are discarded as solid waste and discarding bulk of catalyst can be alarming for the planet [21].Therefore, it is extremely necessary to utilize the coked catalyst in some useful process with or without little fabrication.

1.2.2 Electrolysis of Water

Hydrogen can be obtained from water which due to its abundancy, sustainability and recyclability is the most preferred source. Currently, electrolysis or splitting of water through electricity contributes to about 4% of the hydrogen production [22]. The commercial use of electrolysis can be traced back to 1890.

In electrolysis, the chemical bonds present in water molecules is broken in hydrogen and oxygen. The process of electrolysis is usually done at room temperature. Acidic solution of sulphuric acid as well as alkaline solution of sodium or potassium hydroxide is generally used as an electrolyte while Ag/AgCl as a reference electrode while Platinum (PT) is used as a counter electrode because Pt is usually inert in acidic as well as basic solution [23]. The kinetics of electrolysis reaction in acidic electrolyte are fast and in alkaline electrolyte they are reported to be sluggish [24]. The process of electrolysis is the cleanest process because there are no greenhouse gas emissions. Besides, the formation of hydrogen only oxygen is formed which is also demanding for a variety of industrial applications. The efficiency of water electrolysis for the production of hydrogen is about 60-70% which with daily advancements in development of new catalysts is increasing day by day [25]. While some advancement in the electrolysis have occurred, which includes the electrolysis from solar energy as well as thermal energy.

1.2.3 Photo-electrolysis

The splitting of water through solar energy is in the phase of development which is currently in its experimental phase. It differs from electrolysis only due to the source of energy which breaks the chemical bond of water and the electrode material used through which that bond breaks. The photoelectrode used in photo-electrolysis is usually a semiconductor type material which absorb solar energy while at the same time uses that energy for splitting of water [25]. A photoelectrochemical (PEC) is used for the collection of photons and through these collected photons hydrogen is

generated. This submerged photoelectrode in an electrolyte is exposed to radiation of sun which generate sufficient energy that can be utilized for the production of hydrogen and oxygen [26].During photo electrolysis when hydrogen is produced the electrons are released into the electrolyte while for the production of oxygen electrons are required so if more solar energy is utilized more hydrogen which will be produced more electrons and more oxygen hence increasing the efficiency of photoelectrode. The performance of photoelectrode is evaluated by the overpotential it requires for a current density of 10-30 mA/cm^2 which for a good photoelectrode is reported in the range of about 1.3-1.6 V [27].

1.2.4 Thermochemical electrolysis

In thermochemical water electrolysis heat is used for water splitting [28]. The efficiency of thermochemical electrolysis is reported to be 50% [29]. Usually, the decomposition of water occurs at about 2500 C but by using stable and efficient semipermeable membranes of zirconium oxide and palladium. Different processes are reported for using thermochemical process but in the production of water the main hurdle is of operating at low temperatures because it still requires high pressure to operate and achieve an efficient thermochemical electrolysis [30]. It is conceived that the thermal efficiency of the process can be improved by scaling up the process with developing an understanding of adjusting the thermal efficiency, thermodynamic losses to the capital cost of producing hydrogen [28] .

1.2.5 Mechanism of Electrolysis

The process of electrolysis can be given by reaction of splitting water occurring at anode as well as cathode [31]. The mechanism of electrolysis reaction depends upon the nature of electrolyte. In acidic electrolyte, positive hydrogen ions or protons((intermediate) combine to form hydrogen gas while in alkaline medium hydronium ion (intermediate) yields hydrogen ion [32].The evolution of hydrogen occurs at cathode while the evolution of oxygen occurs at anode. In comparison to acidic media alkaline media allows the usage of non-noble based metal catalyst. The mechanism of water splitting is given below [33].

Acidic Media

At Cathode

$$2H^+ + 2e^- \rightarrow H_2 \qquad (1)$$

At Anode

$$H_2O \rightarrow 2H^+ + 1/2O_2 + 2e^- \qquad (2)$$

Alkaline Media

At cathode

$$2H_2O + 2e^- \rightarrow 2OH^- \qquad (3)$$

At anode

$$2OH^- \rightarrow H_2O + 1/2\ O_2 + 2e^- \qquad (4)$$

1.2.5.1 Hydrogen evolution reaction

The mechanism of HER involves three steps i.e., Tafel step, Volmer step and Heyrovsky step shown in figure (1). In the acidic media protons are reduced while in the alkaline media water molecules are reduced to form hydrogen molecule [34]. In Volmer step (Eq (5) and (6)) a reaction between proton and electron happens which yields an adsorbed hydrogen atom (H^*) on the surface of electrode. The proton sources are water molecules and hydronium ion in the alkaline and acidic media, respectively [35]. Eventually, the Volmer step is followed either by Tafel or Heyrovsky reaction or both [36]. In the Heyrovsky reaction (Eq (7) and (8)), another proton diffuses to the adsorbed hydrogen atom (H^*) and then takes the second electron resulting in evolution of Hydrogen. While in the Tafel step (Eq (9)) two adsorbed hydrogen atoms combine on the electrode surface and yields Hydrogen.

Volmer reaction (Electrochemical Adsorption)

$$H_3O^+ + M + \mathrm{e}^- \Longleftrightarrow M - H^* + H_2O \quad (acidic\ medium) \qquad (5)$$

$$H_2O + M + \mathrm{e}^- \Longleftrightarrow M - H^* + OH^- \quad (alkaline\ medium) \qquad (6)$$

Heyrovsky Step (Electrochemical Desorption)

$$`H^+ + M - H^* + \mathrm{e}^- \Longleftrightarrow H_2 + M \quad (acidic\ medium) \qquad (7)$$

$$H_2O + M - H^* + \mathrm{e}^- \Longleftrightarrow H_2 + OH^- + M \quad (alkaline\ medium) \qquad (8)$$

Tafel Step (Chemical Desorption)

$$2M - H^* \longleftrightarrow H_2 + 2M \ (both\ acidic\ and\ alkaline\ medium) \quad (9)$$

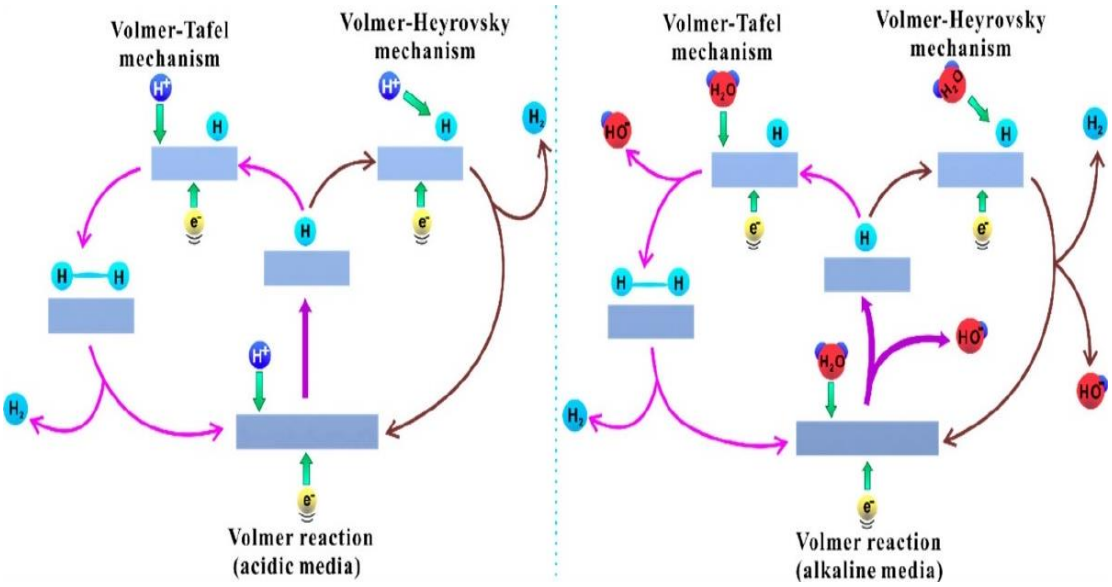

Figure 1 Mechanism of HER on electrode surface in acidic (left) and alkaline (right) medium. Reprinted with permission from ref [37].

The Tafel slope shows the difference of potential which is required to for increasing or decreasing the current density by 10 folds. It can be found by plotting a graph between overpotential and log of current density obtained from the linear sweep voltammetry.

Chapter No. 2

Literature Review

The most facile process used to obtain hydrogen is through water splitting. Electrolysis is the most sustainable path because water as feed stock is abundant and renewable source for hydrogen production [38]. However, the electrolysis process can be traced back to late 18 century but still the main hurdle which limits the widespread practical application of electrolysis is its high cost. The main factor which makes electrolysis cost-hefty is the development of electrocatalyst. In spite of high electrochemical performance the conventionally used noble metal Pt, IrO_2 and RuO_2-based catalysts are avoided due to terrestrial scarcity and high material cost [39–43].

2.1 Transition Metal Dichalcogenides

Recently, robust, earth abundant and cheap transition metal dichalcogenides (TMDs) having a general formula MX2 (M = Transition metal, X = Chalcogen), have been uncovered, showing promising electrocatalytic activity]. Amidst these TMDs, MoS2 have grabbed attention of the researchers due to high theoretical catalytic activity, low cost and greater electrochemical stability [44–46].

2.2 MoS_2 as an electrocatalyst

Initially, MoS_2 bulk was considered as non-reactive for HER but in 2005 with the finding that hydrogen bonding computational free energy of MoS_2 edges i.e. ΔG_{H^*} of Mo ($\bar{1}010$) edge site of MoS_2 at about 50% coverage of hydrogen is about 0.08 eV [47]. This ΔG_{H^*} of Mo is considered to be similar to that of Platinum ($\Delta G_{H^*} \approx 0$) which raised the possibility of MoS_2 as a catalyst for HER. This study also experimented with nanoparticles of MoS_2 for which graphite was used as support material. Generally, there are about three different kinds of arrangements in which MoS_2 can be categorized. The polymorphs of MoS_2 can be 2H (hexagonal), 1T (Trigonal), 3R(rhombohedral). The 2H consists of two layers per unit cell with MoS_6 trigonal prism edge -sharing. While the metastable 1T MoS_2 have an octahedral coordination of molybdenum with one layer per unit cell. 2H and 1T polymorphs are widely used due to their catalytic activity. After the study of that various sized MoS_2 were prepared

with different molecular structure and different arrangements of nanosheet have been engineered [48]. However, it is well known that the two major constraints that limits the further enhancement of MoS_2 activity are the low electrical conductivity and highly inert basal plane of MoS_2 [49–51]. These shortcomings have been curbed through immense research in which the 2H-MoS_2 (i.e. semiconductor with a band gap of about 1.9 eV) is replaced with nano-structured 1T-MoS_2 with 10^7 times more conductive because the 4D orbital in 1T-MoS_2 is incompletely filled [52,53]. Supporting MoS_2 with highly conductive nano-materials like graphene sheet [54], carbon nanospheres [55],carbon , nanocages [57], and nanofibers [58], further aids to the enhancement of HER and OER performance.

2.2.1 Edge sites enhancement in MoS_2

The HER activity of MoS_2 can be enhanced by exposing the edges per unit area through structural downsizing with various morphologies like nanoflakes, nanosheets, nanowires, and so on. For example, a template of silica with double-gyroid (DG) was used for synthesizing thin nanofilms of MoS_2 due to which the active edges of MoS_2 were exposed acknowledging highly curved surface and bi-continuous-nano porous network of MoS_2 which greatly increased the HER activity [59]. On a fused layer of silica, a single layered fractal shaped MoS_2 were also produced which possessed ample active sites confirming the enhancement of HER performance by exposing more edge sites [60]. Vertically aligned MoS_2 were also grown on the substrate of Mo by beam evaporation and after that the HER activity of compared to that of edge sites [61]. Similarly, single crystal MoS_2stacked in parallel in which the top surface was covered by edge sites and the basal plane was vertically arranged also gave promising HER results [62].

In one study on a conductive carbon fiber paper the nanosheets of MoS_2 were vertically arranged which showed a ΔG_{H^*}=0.02eV achieving a current density of 10 mA/cm^2 at an overpotential of 104 mV with greater stability [63].

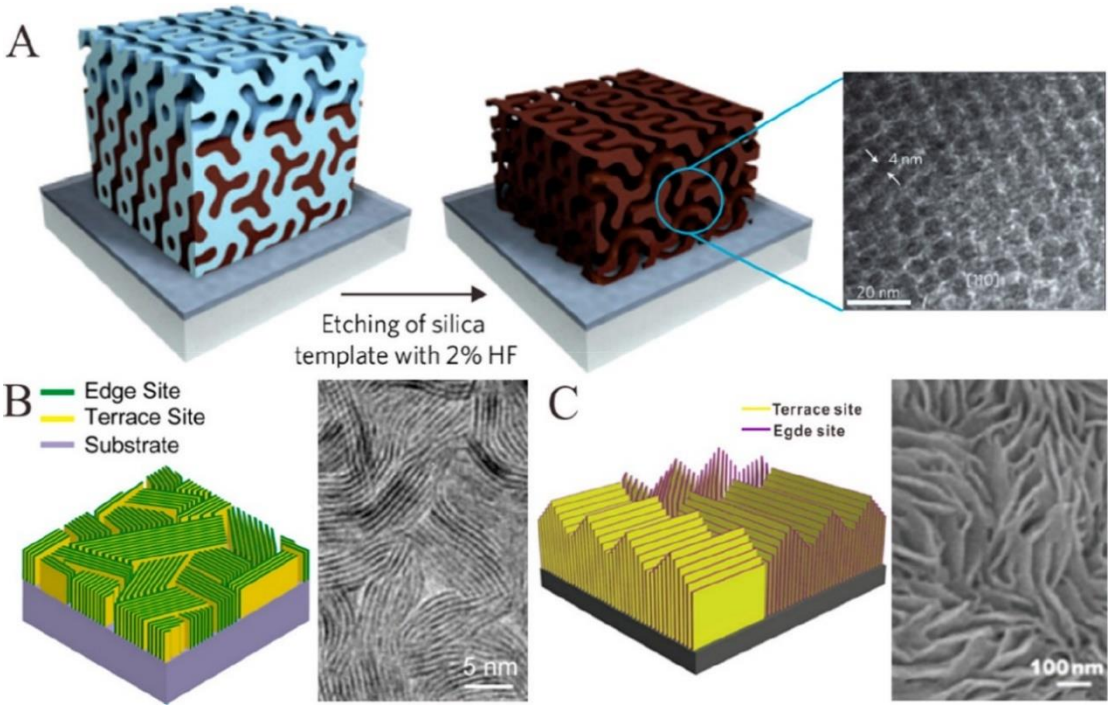

Figure 2 (A) Synthesis process of DG mesoporous MoS_2 (with TEM images) (B) MoS_2 perpendicularly aligned films. (C) MoS_2 possessing vertically aligned stepped-edge surface-terminated. Reproduced with permission from ref [59,63]

2.2.2 Engineering Defects and strains

It is considered that as the basal plane makes a large portion of MoS_2 due to which the basal plane is thermodynamically more stable than the edged plane of MoS_2 [64]. As the edges sites comprises of unsaturated Sulphur atoms which enhances HER activity therefore, defects in the structure of basal plane of MoS_2 can be created intentionally. It has been observed that a lot of research has been carried out for creating Sulphur vacancies [65,66] An experiment of a concentrated precursor with superfluous thiourea was used by Xie et al, this thiourea not only helped to transform Mo^{6+} to Mo^{4+} but also acted as an additive for stabilizing the ultra-thinMoS_2 thus delivering an onset potential of 120 mV as shown in figure 3 (A) and (B) [67]. This work inspired another work in which the concentration of S vacancies were regulated via tuning of solution source in hydrothermal process [68–71]. Moreover, treatment of ultrathin 2H MoS_2 through Ar plasma generate S vacancies of tunable levels with strains and concentrations which allows the bonding of hydrogen to the exposed molybdenum atoms hence playing a role in activation of basal plane. By evaluating the electronic structure of 2H MoS_2 this study revealed that a new Fermi level can be created by the sulfur vacancies and increase in the tensile strain and these vacancies could shift the band position more closer to Fermi level as shown in figure 4 (C-F) [66]. It is revealed from the kinetic

study that the S vacancies and out of plane tensile strains can have a huge impact on the enhancement of HER activity [72]. On large scale, desulphurization through electrochemical method can be used for the S-vacancy complemented 2H $MoS_2$by varying desulphurization potentials to a desirable extent of tuning which means the HER performance of the MoS_2 can be tuned [73]. A recent study conducted by Li and coworkers achieved a current density of 10 mA/cm^{2}with an overpotential of 136mV by depositing nanocrystals of unsaturated 3D ordered-edged enriched MoS_2on carbon cloth hence, enhancing the stability and catalytic activity for HER [74].Another study reported that developing a linkage between dithiolene (Mo_3S_7) and thiolate helped in the improvement of catalyst loading and turnover frequency and this catalyst required and overpotential of about 89mV to attain a current density of 10 mA/cm^2 [75].

For manipulation of structure and catalytic performance of HER another significant approach is doping. The density functional theory revealed that doping of cobalt in MoS_2 edges decreased the S-edge ΔG_{H^*} to 0.10 eV from 0.18 e without changing the Mo-edges thus showing that by incorporating Co dopants the S-edges can be activated [76].Similarly, this work paved the pathway for using other noble-metal based dopants like Pt, Pd, Ru and Au [65,77–79], non-noble metal-based dopants like Co, Fe, V, Zn, Cu and Ni [80–86] and nonmetal based like O, B, N and P [87–90]in the basal or edge plane of $MoS_2$for promoting HER. Comparably, a demonstration by Zhang et al showed through doping of Ni in the nanosheets of crystalline MoS_2 an acceleration in the kinetics of HER. The same enhancement in the HER kinetics was shown by doping Co and Fe in the MoS_2. Xie's group showed an increase in the conductivity and regulation of electronic structure by doping O in the MoS_2via modifying the conduction and valence band densities [88]. Using P as dopant also revealed a phenomenally low overpotential of 43 mV at a current density of 10 mA/cm^2. These results were accredited due to the doping of P in the MoS_2in which P played a part in developing active sites and increasing the spacing between interlayers of MoS_2 thus,

enhancing HER [90].

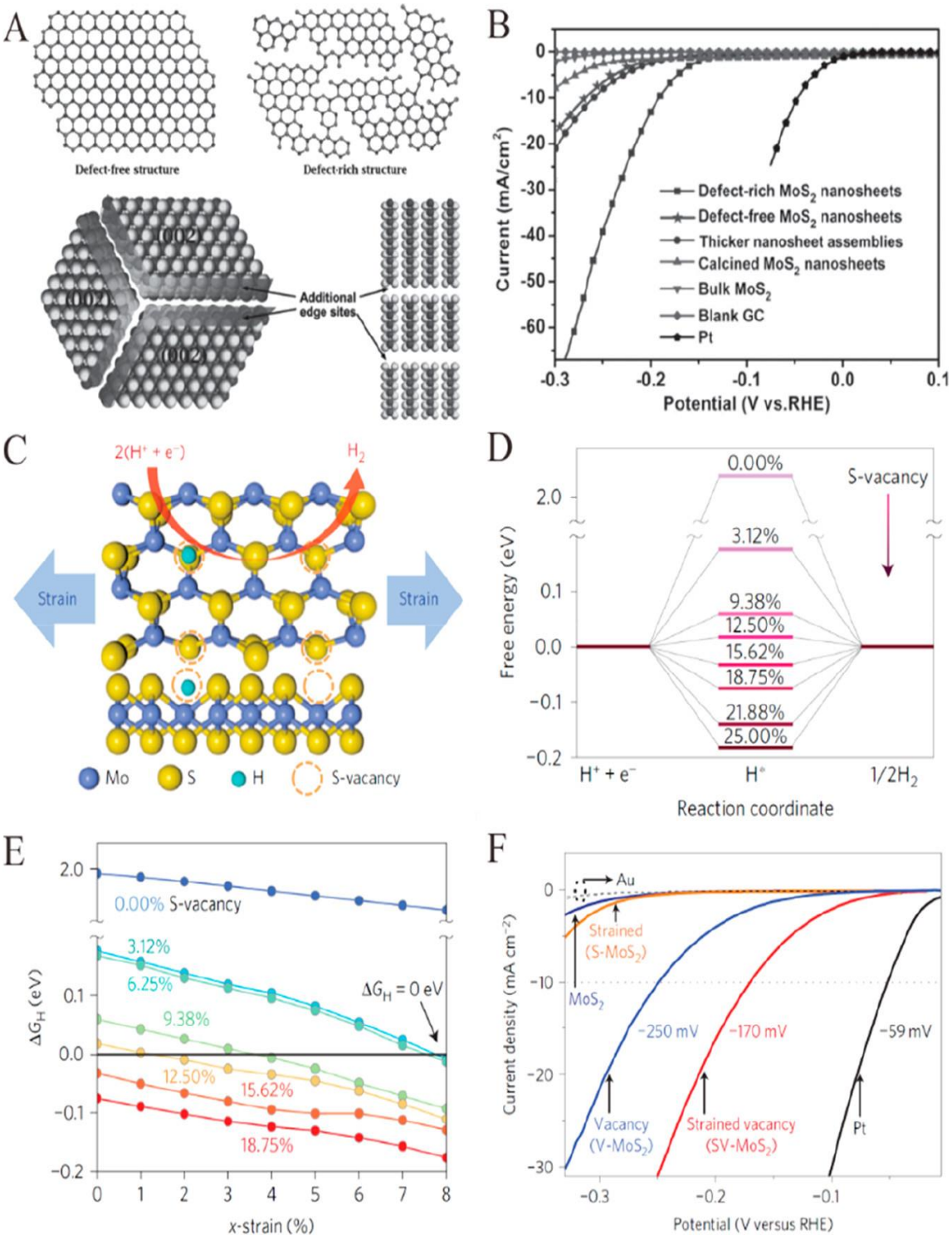

Figure 3 (A) MoS2 nanosheet with and without defects with (B) LSV for HER. (C-F) Ar plasma generated S vacancies at tunable levels with new fermi level generations. Reproduced with permission from ref [66,67].

2.2.3 Tuning of phase

As revealed earlier, the characteristics of 2H MoS_2 are that of a semiconductor i.e., the electron transport is limited within it. Comparatively the structure of 1T MoS_2

possesses metallic nature which are known to be good conductors for electron transport [53,91,92]. The band gap computational analysis showed that 1T MoS_2 have a band gap of 0.06 which is relatively very less as compared to 2H MoS_2which is1.74 eV [91]. Lukowski et approved by obtaining 1T MoS_2 from experimental exfoliating 2H moS_2which was grown on graphite via n-butyl lithium intercalation that 1T MoS_2 have improved electrode kinetics, more active sites, and low electrical transport loss as compared to 2H MoS_2 [93]. It is shown by theoretical investigations that Volmer-Heyrovsky mechanism is followed by 1T MoS_2 and comparably the edges of Mo in 1T have better charge transfer kinetics to that of MoS_2as shown in figure 4(A)and (B) [94]. Similarly, Wang et al. experimented with electrochemical lithium-ion intercalation which was performed under controlled potentials so that the conversion from 2H to 1T can be tuned continuously. After that, a study was conducted by Voiry and co-workers in which they synthesized 1T MoS_2 by a solvent free intercalation method which on comparison of catalytic activity before and after oxidation revealed that it is not the edges but the basal plane that possessed main active sites hence resulting in the Tafel slope of about 40 mV/dec [95]. Attanayake et al enhanced the HER performance by introducing ions of metal which were compatible to the theoretical results [96]. Furthermore, a facile pathway comprising of lithium intercalation and ball milling was reported for largescale production and greater yield of 1T nanodots was reported which reported 10 mA/cm^2 at an overpotential of about 140 mV [97]. A very recent study also reported the synthesis of MoS_2 via hydrothermal method followed by annealing which resulted in abundant 1T phases and large number of active sites this was prepared from a complex of thiourea and melamine-phosphomolybdate [98].

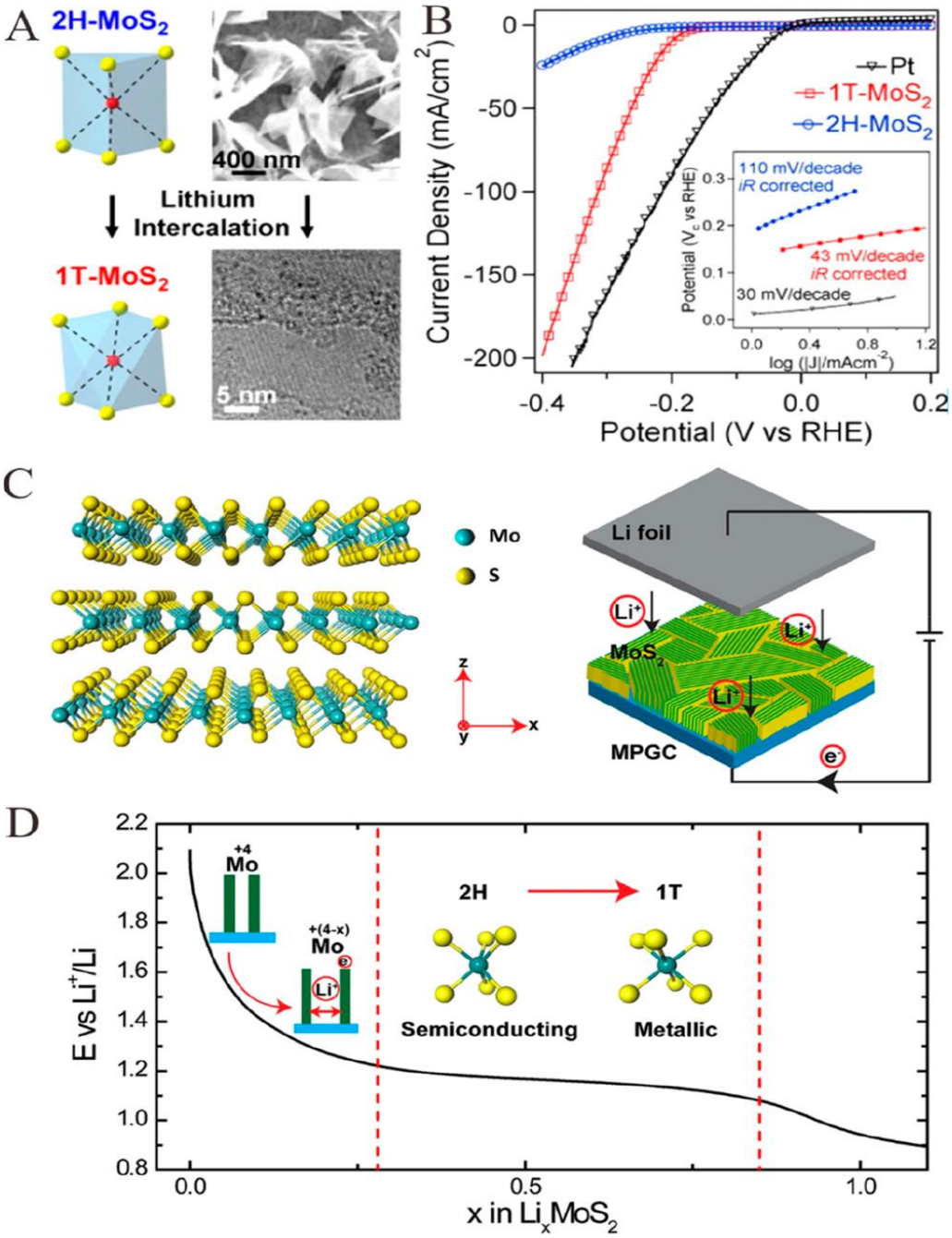

Figure 4 (A) Conversion of phase from 2H MoS2 to 1T MoS2. (B) Schematics of Li intercalation into MoS_2 nanofilms and their corresponding galvanostatic discharge curve. (Upper panel) Structure of crystalline 2H MoS_2 and battery testing system. Anode of Li foil (Lower panel.) Reproduced with permission from [81,93].

2.2.4 Construction of heterostructure

Coupling of conductive phase(s) with an electrocatalyst if the most regularly used and commonly practicable method for achieving or enhancing the conductivity for electrochemical performance. Li et al had a breakthrough by using ammonium tetra thiomolybdate supported by graphene oxide. The coupling of graphene oxide with the precursor of Mo exhibited ample active edges with an electrical coupling with GO. On comparing it with bare MoS_2 the MoS_2 on GO showed boosted electronic conductivity with high HER performance and greater stability [99]. Moreover, some studies showed that the coupling of conductive material not only amplify the conductivity but also adjust the value of ΔG_{H^*} [100,101]. Afterwards, different kind of materials like mesoporous foam of graphene [102], porous carbon [74,103–106]carbon nanospheres [107], nanotubes of carbon [108,109] cloth of carbon [110–112], and carbon fiber [113,114] were tested by coupling it with MoS_2 which showed advancements in HER activity. Besides, materials that were carbon based other materials with good conductivity like oxides [115,116], metals [117,118], sulphides [119–122], carbides [123–125], nitrides [126], selenides [127,128] were used for coupling with MoS_2 which also showed enhanced HER performance.

2.3 Our work

We obtained methane reforming catalyst composed of manganese (Mn), nickel (Ni) and Aluminum (Al). These Mn, Ni, and Al were combined in different ratios to synthesize a layered double hydrotalcite. The MnNiAl LDH was synthesized by co-precipitation with about 15, 40 and 65 % loading of Nickle and tested for methane decomposition. The calcination at different temperatures revealed the effect of carbon grown on the surface of the catalyst. Different morphologies of carbon were formed which was dependent on the Nickle loading in the ex-hydrotalcite. The study of different temperatures showed that the concentration of Nickle affected of carbon formation. The ex-LDH with 40% showed greater stability in the temperature range of 500-750 C but still it eventually got deactivated by carbon developed on its surface. It was concluded that a spinel like structure was developed from ex-hydrotalcite with 40% Nickle and when the ratio of Nickle was decreased graphitic carbon was developed on the surface of these catalyst. Instead of wasting the spent ex-LDH catalyst with Graphitic Carbon (GC) and carbon fibers (CNFs) they were utilized for electrolysis of water.

In this research we took the spent methane reforming catalyst with GC and CNF and used it as a support for MoS_2. As mentioned, above the main hurdle for using $MoS_2$is the inert basal plane. Therefore, it was envisioned that such an electrocatalyst should be developed which with providing better catalytic performance and stability should also be highly conductive for which purpose this research of in-situ synthesizing a heterostructure of active edged MoS_2 and conductive carbon from spent methane reforming catalyst was developed.

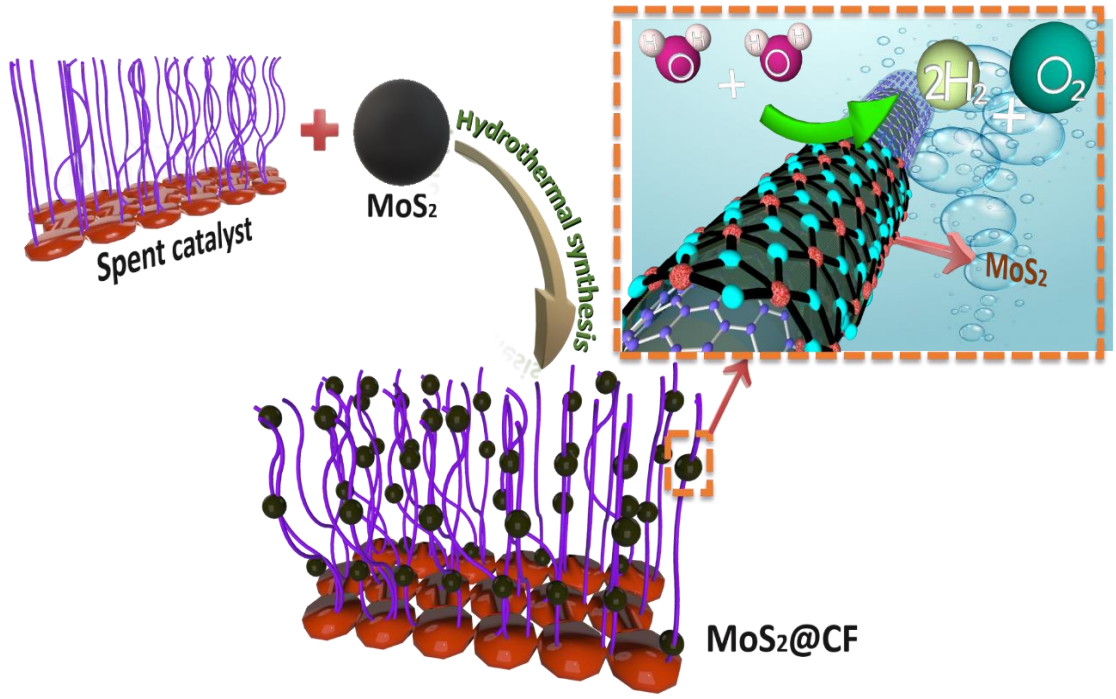

Figure 5 Schematic illustration for utilizing spent reforming catalyst for electrochemical water splitting.

Chapter No. 4

Methodology

4.1 Materials used in synthesis of catalyst.

Ammonium heptamolybdate $(NH_4)_6Mo_7O_{24}.4H_2O$, CAS number: 12054-82-2 (purity= 99.0%) was purchased from DAEJUNG. Thioacetamide (C_2H_2NS) reagent grade, CAS number: 62-55-5 was purchased from SCHARLU. Ni Foam (>99.0%) was purchased from Sigma Aldrich) acetone (>99.8%, VWR Chemicals), ethanol (>99.9%, Lab scan Asia Co. Ltd),

4.2 Experimentation

4.2.1 Preparation of Spent catalyst

The final fabricated composite of MoS_2 on spent catalyst was synthesized by adopting in-situ hydrothermal method. This method involved the synthesis of final composite via in-process growth of MoS_2 on spent catalyst. 1.4 mmol of ammonium heptamolybdate and 22.9 mmol of thioacetamide were dissolved in about 50 ml DI water. 3 ml of Hydrazine hydrate was added to the solution drop wise. For maintaining pH of the solution hydrogen chloride (HCl) was added to the solution. About 1g of spent catalyst was added to the mixture. After vigorous stirring for about 2h at 800 RPM the mixture was transferred to Teflon-lined autoclave which was then heated at 200 ˚C for about 24 h. The autoclave was allowed to cool naturally under room temperature. The resulting black mixture was sonicated, centrifuged, and washed with ethanol and DI water after which it was dried overnight at 80 ˚C. In this process MoS_2 was obtained from the reaction of $(NH_4)_6Mo_7O_{24}.4H_2O$ and C_2H_2NS with water. Ammonium heptamolybdate served as a source of Molybdenum while thioacetamide provided the Sulphur required. Following reactions occurred forming intercalated MoS_2 [129].

$$C_2H_2NS + 2H_2O \longrightarrow CO_{2\,(g)} + 2NH_{3(g)} + H_2S \quad (1)$$

$$(NH_4)_6Mo_7O_{24} + 28H_2S + 8NH_3 \longrightarrow 7(NH_4)_2Mo_4 + 24H_2O \quad (2)$$

$$(NH_4)_2Mo_4 + 2N_2H_4 \longrightarrow MoS_2 + 2N_{2(g)} + (NH_4)_6S \quad (3)$$

4.2.2 Preparation of ink and Synthesis of electrode

The ink for electrochemical testing was prepared by taking sample of decorated spent catalyst, carbon black and PVDF in a ratio of 85:10:5 respectively. Firstly, the PVDF was sonicated in NMP for about 2h. Then carbon black and prepared sample was added and again sonicated for about 4h which resulted in black ink. About 50 µl of the prepared ink was taken with the help of micro-pipette and then deposited on treated Nickle foam of area 1 cm^2. Nickle foam was used as substrate, which was treated by sonicating it in acetone, then in 2 M HCl and lastly in absolute ethanol, consecutively, for 15 minutes in each solution. The drying of Ni foam was done at 60 ˚C in a drying oven for 2 h. The ink-loaded foam was dried at 80 ˚C for about 12h. The loading on nickel foam was noted by weighing it before and after deposition of ink which varied from 2.1 mg to 2.8 mg for all samples and this variation was due to change is density of samples before and after deposition.

4.3 Techniques used for electrode characterization.

STOE-Seifert X'Pert PRO was used for XRD characterization while 2θ value ranged from 5˚ to 80˚ using Cu-kα radiation. Morphological characterization was done by Scanning Electron Microscopy and EDX mapping for which SJEOLinstrument JSM-6490A was used. Analytical information was studied by Fourier Transform infrared spectroscopy (FTIR) for which iS50 FT-IR spectrometer, Thermo Scientific was used. Electrochemical testing of the sample was performed by using Biologic potentiostat with three electrodes cell. Platinum (Pt) gauze was used as counter electrode while Ag/AgCl was used as a reference electrode. The prepared loaded Ni foam was used as working electrode. 1M potassium hydroxide (KOH) was used as electrolyte. Cyclic voltammetry (CV) was performed at 10, 20, 40, and 50 mVs^{-1} in a voltage range of -0.4 to 0.6 V. For ease and further calculations reversible hydrogen electrode potential was used which was obtained using $E_{RHE} = E_{Ag/AgCl} + 0.059pH + 0.1976$, with pH = 14. For computing resistance, the electrochemical impedance spectroscope (EIS) frequency was kept between 200 KHz and 100 MHz with alternating voltage amplitude of 10 mV. To avoid the misinterpretation of rate determining step large overpotential region is considered and all the above-mentioned parameters were obtained from the quasi-steady state polarization curves of HER which were *iR*-correction from impedance data.

4.3.1 Scanning electron microscopy (SEM)

For morphological analysis of spent and synthesized catalyst scanning electron microscopy was used. Before analysis, our material was kept on a stud and then coated with gold for giving it a conductive layer.

4.3.1.1 Objectives

For analyzing the material surface and formation of MoS_2SEM is an outstanding technique. It can give a detail information about

1.) The external morphology of material
2.) The orientation of material formed.
3.) The crystallinity of a substance

4.3.1.2 Working Principle

An electron beam is used which produces the morphological image of the tested material while different magnifications are obtained through altering electromagnetic fields.

4.3.1.3 Components

Following are the components of SEM.

1.) Source of electron beam
2.) Condenser lens
3.) Scan coils
4.) Objective lens
5.) Secondary electron detector

Electrons are generated from an electron source which are shaped into a beam. The emitted electrons catch acceleration through the accelerator and attracted towards the anode. The beam's diameter is adjusted using condenser lens. On weaking of this beam another broader beam is produced. A lens controls the path of electron and an electromagnetic lens comes in action if the electrons are unable to pass through the glass. After convergence of condenser lens the electron beam passes to the objective lens from where a secondary electron detector captures the image and sends it to display.

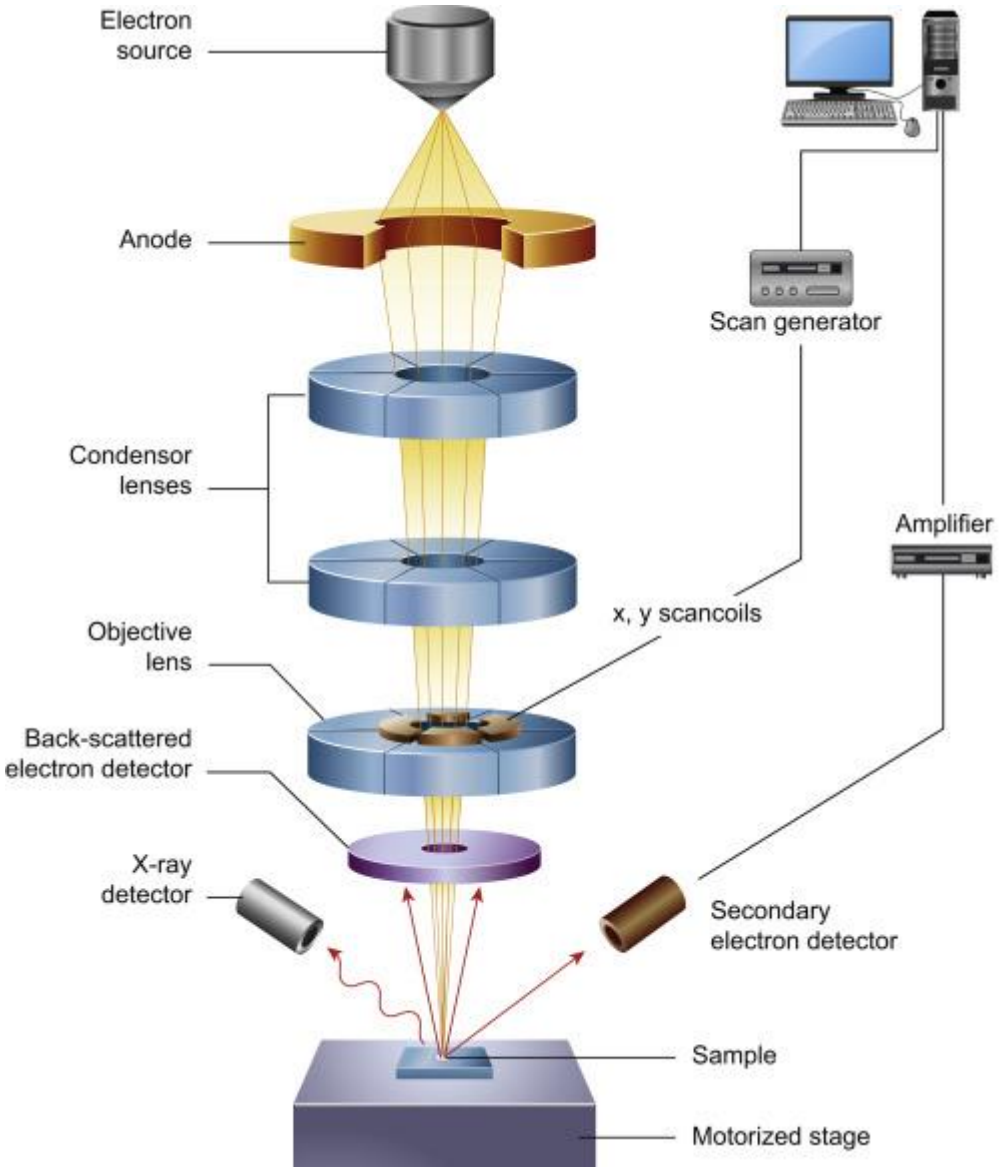

Figure 6 Working of SEM. Reprinted with permission from ref [130]

4.3.2 Energy dispersive X-ray Spectroscopy (EDS)

EDS is a technique used for analysis of elemental composition of a sample. Point mapping and area mapping are the techniques used in EDS for analyzing the detailed composition of any material.

4.3.2.1 Working Principle

It works on the principle of dissipation of incident X-rays energy by creating a series of electron-hole pairs in the material. Across the crystal, a voltage is applied which pushes holes and electrons toward the opposite side of the crystal resulting in signal which is send to the pulse detector. The signal size is directly proportional to the incident X-ray. From the measurement of current amount that incident X-ray photon

produces, we can calculate the energy of the original X-rays. At each energy the number of X-rays measured generates a histogram which can be seen in the form of a EDS spectrum.

4.3.2.2 Components

1.) Collimator
2.) Electron Trap
3.) Window
4.) Crystal detector
5.) Detector

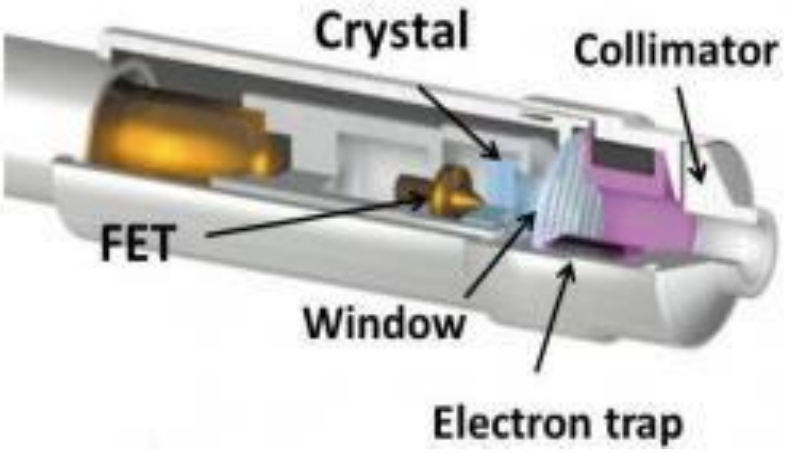

Figure 7 Components of EDS

A collimator is used for ensuring the collection of X-ray generated only form the interaction of electron beam with the sample. An electron trap allows only the entrance of X-rays to the detector. Passing from the window the X-rays enters to the detector which converts the signal to a pulse voltage and the pulse is displayed in the shape of spectrum on the display.

4.3.3 Fourier Transform Infrared spectroscopy (FTIR)

This technique is used for studying the interactions between two phases of a material from studying which one can know about the formation of their desired material. For analysis of our sample, we used ATR-FTIR which carried out the analysis on scanning frequency of 32 Hz with a given wavenumber range of 500-4000cm^{-1} at 4cm^{-1} resolution.

4.3.3.1 Objectives

Following are the objectives of FTIR.

1.) Identification of functional groups present in the materials which may be recognized as organic, inorganic, and polymeric.
2.) Finding the presence of contamination or undesired substance
3.) Knowing about any unknown material
4.) Decomposition, uncured material, and oxidized substances can also be identified in failure analysis.

4.3.3.2 Working Principle

An incident light, which belongs to an infrared and electromagnetic region is absorbed by molecules. Each molecule or functional group have unique absorbance of light according to the bond present between them. The region of infrared is in between 12800cm^{-1} to 10 cm^{-1}. The absorption spectrum depends on the bonds present between molecules which can show vibration, rotation and stretching if the incident light is absorbed by the molecules. A disturbance in the behavior which is in the form of dipole movement indicates the nature of bond and functional group present in the material.

4.3.3.3 Components

Following are the basic components of FTIR.

1.) Source of Infrared light
2.) Interferometer
3.) Sample placement area
4.) Detector
5.) Amplifier
6.) A/D converter
7.) Computer

The source of IR generates and emits radiations which after passing through the interferometer strikes the samples. Some light is absorbed while other passes from the sample which is then detected by the detector. An amplifier amplifies the final signals and send it the analog to digital converter. Eventually, the signal is transferred to a computer which displays the spectrum of absorption and the presence of functional groups.

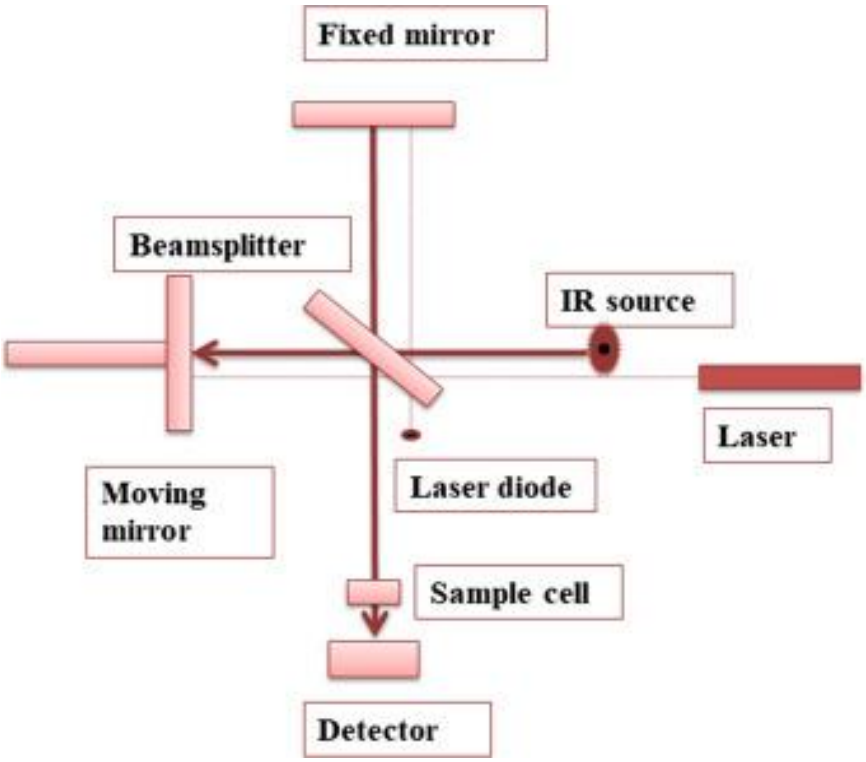

Figure 8 Components of FTIR

4.4 X-ray diffraction spectroscopy

STOE-Seifert X'Pert PRO was used for obtaining XRD spectrum of spent catalyst and synthesized catalysts. About 40 KV voltage with a current of 40 mA was applied. A step size of 0.04 was used with a step time of 0.5s/step. An angle in the range from 10^{o-} to 80^{o} was used.

4.4.1.1 Objectives

The main objective of XRD is for

1.) Identification of crystalline structures
2.) Differentiating in between difference forms of a structure
3.) Calculating the distance between lattices
4.) Finding the particle size

4.4.1.2 Working principle

It works on the constructive interference between x-rays. A cathode ray tube is used for the production of radiations.

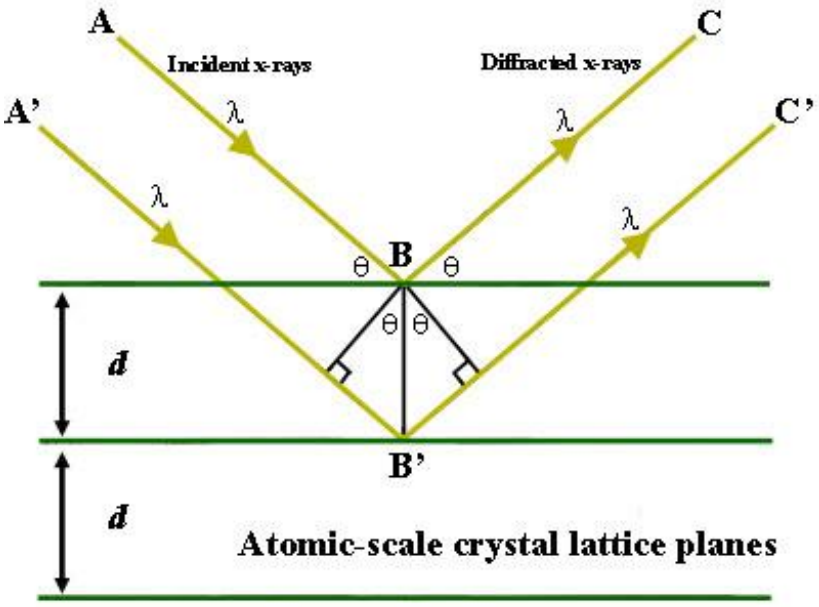

Figure 9 Schematics of XRD

The interaction of specimen and rays interfere constructively according to Bragg's law which states that there is a direct relationship between wavelength of radiations used and the distance between lattice spacing and diffraction angle that is the angle between the incident and diffracted rays. The Bragg' s law is given mathematically as

$$n\lambda = 2dsin\theta$$

where n stands for the order in which reflection occur, λ represents the wavelength of electromagnetic radiations. D is the lattice spacing between crystal planes of a sample while θ is the angle between X-ray beam and the crystalline phase of sample.

Chapter No. 5

Results and discussion

5.1 Morphological Characterization

The morphological characterization of the spent methane reforming catalyst was performed using Field emission scanning electron microscopy (FESEM), X-ray diffraction spectroscopy (XRD) and Fourier transform Infrared Spectroscopy (FT-IR)

5.1.1 Field Emission Scanning Electron Microscopy

The scanning electron microscopy provided an insight regarding the microstructure of graphitic carbon (GC) and CNF grown over the spent catalyst.

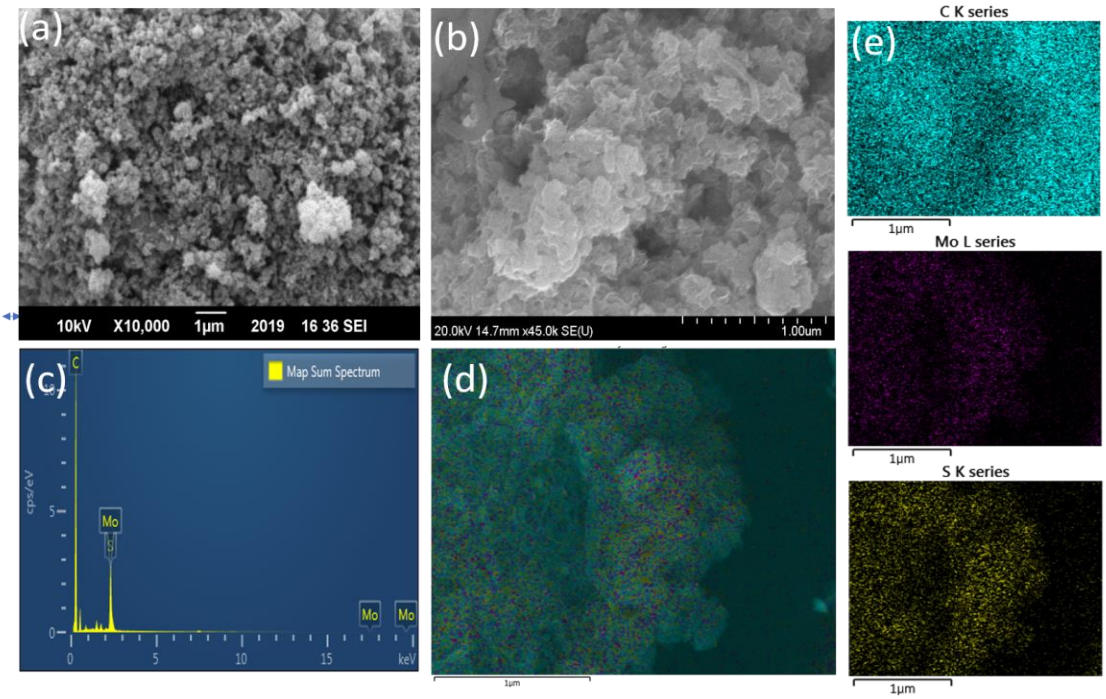

Figure 10 (a) SEM image of spent methane reforming catalyst with Graphitic Carbon (GC), (b) FESEM of spent catalyst after deposition of MoS_2 i.e., MoS_2@GC, (c) EDS elemental distribution graph for MoS_2@GC (d-e) EDS elemental mapping of MoS_2@GC.

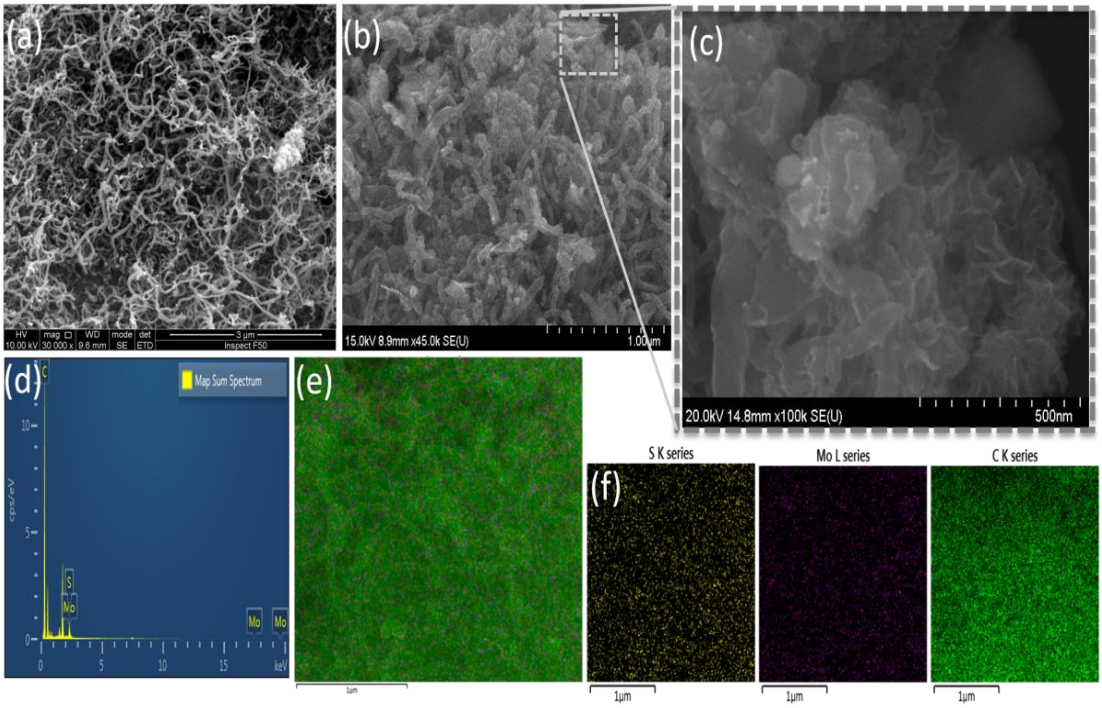

Figure 11 (a) FESEM images of spent methane reforming catalyst with Carbon nanofibers (CNF) (b) FESEM image of MoS_2 nanoflakes deposited on CNF (d) EDS elemental distribution graph for MoS_2@CNF (e-f) EDS elemental mapping of MoS_2@CNF.

Energy dispersive spectroscopy (EDS) point mapping (figure 3 (c) of MoS_2@GC shows the highest peak of 11 cps/eV for carbon with definite peaks of Mo and S, while the area mapping shows deposition of MoS_2 on the graphitic carbon.

Similarly, in figure 7 (b) carbon fibers with deposits can be seen while innumerable thin nano-flakes of >100 nm in size are visible in high magnification FESEM image (figure 7 (c)). Furthermore, the EDS mapping of one of the larger aggregates under the corresponding FESEM conditions indicates the homogeneous distribution of Carbon (C), Molybdenum (Mo) and Sulphur (S) (figure 7 (e-f). The atomic percent of C, Mo, and S is 99.84 %, 0.11% and 0.05% respectively, which altogether sum up to give a total of 100. From the atomic percent, ratio of Mo and S which is 1:2 confirms the formation of pure MoS_2 ruling out the presence of any other compound of Molybdenum and Sulphur. Another important aspect which can be highlighted from the weight percent of Mo, S and C in MoS_2@GC MoS_2@CNF is the possibility of revitalization and enhancement in performance of spent catalysts with minimal usage of material to be deposited.

5.1.2 X-ray Diffraction Spectroscopy

Successful deposition of MoS_2 on spent catalyst was done using environment friendly hydrothermal process which can be confirmed through XRD. The crystalline phase of the spent catalyst and MoS_2 deposited on spent catalyst was determined using XRD, the spectrum of which is shown in figure 8. The peaks of spent catalyst at 19,29,33,43,55 (JCPDFN-78-552) could be indexed to double layered hydrotalcites with spinel-like structure while the peaks at 12.1,23,34 are associated to planer [131,132]. The peak common in all samples at 2θ= 44 and 2θ=51.7 corresponds to Ni(111) and Ni(200), respectively, embedded in the spent catalyst as well as present at the tip of fibers [132]. A distinguishable peak splitting in the diffraction pattern of all samples at $\sim 26.1^{\circ}$ is attributed to (002) plane of carbon fiber and graphite formation (coking) after the calcination of Hydrotalcite which caused degeneration of catalyst [58,133].

In the pattern of MoS_2@GC and MoS_2@CNF some prominent new peaks at 7.9°,32.7° and 58° appeared which indicates the formation of (001), (100) and (110) planes of single phase MoS_2 ,according to the standard powdered diffraction file JCPDS 37-1492 [134]. The appearance of these peaks with the absence of (002) plane at $2\theta = 14^{\circ}$ confirms the formation of partially exfoliated unstacked mono layered MoS_2 [135,136]. Most peaks that appeared in GC and CNF also appeared in the MoS_2@GC and MoS_2@CNF but a visible decrease in peak intensity and peak positioning was observed. This suppression in the intensity of peaks can be attributed to the exfoliation of graphene and carbon nanofibers during synthesis and successful deposition of MoS_2 over the spent catalyst which are accredited and supported by electron microscopy images [137,138].

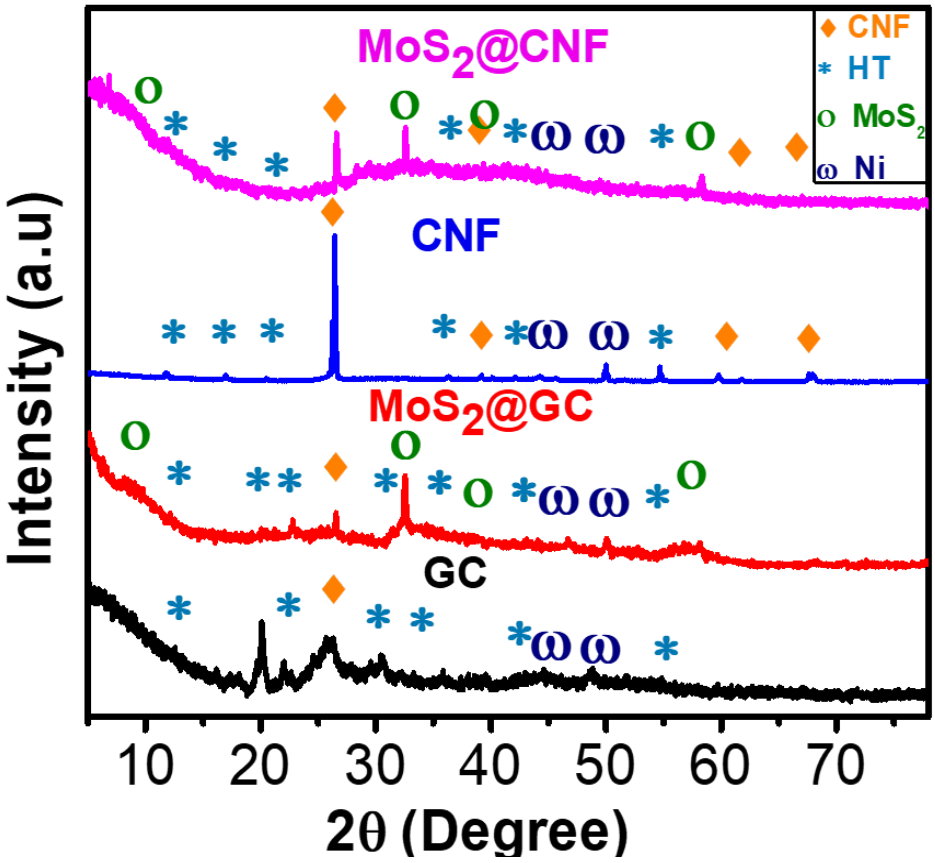

Figure 12 XRD spectrum of GC, CNF, MoS_2@GC, and MoS_2@CNF.

5.1.3 Fourier Transform Infrared Spectroscopy

Chemical structures of MoS_2, spent GC, CNF and newly formed MoS_2@CNF and MoS_2@GC were studied by FT-IR for acquiring the stretching and bending vibrations of functional groups in the samples as shown in figure 9. In the spectrum of MoS_2, MoS_2@CNF and MoS_2@GC hybrids the perceptible peaks at 589 cm^{-1}, 880 cm^{-1} to 960$cm^{-1}$and, 1633 $cm^{-1}$to 1637 cm^{-1} delineates the Mo-S, S-S and Mo-O stretching vibrations, respectively, depicting the formation of MoS_2 [51,139] In the spectrum of CNF and GC the peak at 1198 cm^{-1} can be attributed to the stretching vibrations of carboxylic group which indicates the growth of carbon fibers and graphitic carbon on the spent catalyst while the peak at 1400 cm^{-1} depicts the disarranged structure of interlayered spent catalyst with O-H bend which was further disordered by hydrothermal treatment providing more surface area where MoS_2 can get [140,141]. The adsorption band at 3445 cm^{-1} is associated with the stretching vibration of hydroxyl (0-H) functional group the intensity of O-H stretching is reduced in the hybrids because more MoS_2 was formed. The hydrazine hydrate used in the synthesis

process acted as a reducing agent which removed the water molecules from the hybrids resulting in lowering of O-H transmittance.

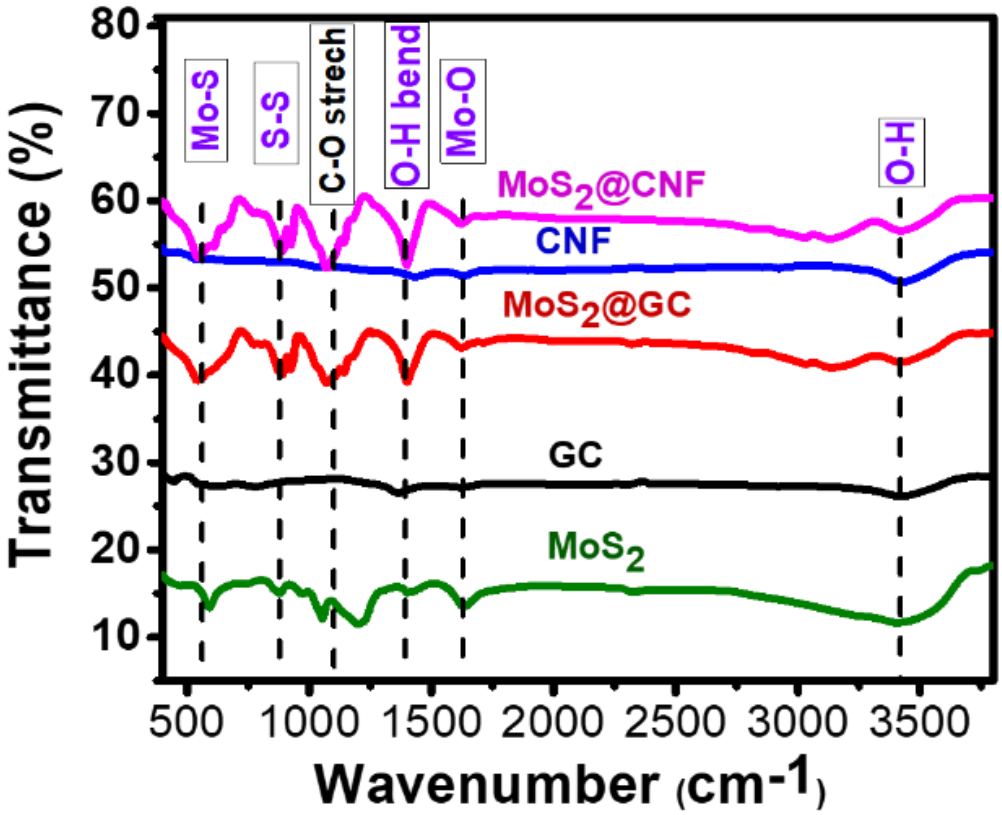

Figure 13 FT-IR spectrum of spent methane reforming catalyst with MoS_2, GC, CNF, MoS_2@GC and MoS_2@CNF.

The increase in absorbance intensity of peaks in MoS_2@CNF and MoS_2@GC hybrids also clearly indicates the deposition of MoS_2 on the surface of spent catalyst which is supports by laudable increase in electrochemical activity of both newly fabricated catalyst. The performance of spent and newly fabricated electrocatalysts can be ascertained by performing electrochemical characterization.

5.2 Electrochemical Characterization

5.2.1 Hydrogen evolution reaction

The HER performance of all the samples was evaluated in 1 M potassium hydroxide which was used as an electrolyte and the scan rate for LSV was kept at 10 mV/s for all samples. The HER performance of a catalyst in alkaline medium is influenced by four major factors i.e., adsorption of water on active sites, ability of catalyst to dissociate adsorbed water, binding energy of hydrogen produced, adsorption strength of aqueous OH^-. For knowing about the performance of an electrocatalyst these factors are

measured in terms of different parameters used in the modified Butler-Volmer equation i.e., $\eta = \pm A\log_{10}(j/j_{\circ})$ which when generalized, gives Tafel equation (i.e., $\eta = \alpha + b\log j$; where α and b are the Transfer coefficient and Tafel slope, respectively) [51]. The parameters used in the above equation are defined and analyzed below i.e.

- Over-potential [(η) (V)] i.e. The difference between electrode potential (E) and standard potential (E°); Over potential required for sustaining a current density of 10 mA cm^{-2} (η_{10}) is usually reported.
- Tafel slope (b) ($V\ dec^{-1}$) i.e., Slope of linear approximation of η vs log of current density.
- Exchange current density [i° (mA cm^{-2})] i.e. Even in the absence of current, a dynamic equilibrium exists at the electrode/electrolyte interface which results in exchange of current density.
- Mass weighed HER current density [($i^{\circ}_{0.2}$) (Ag^{-1}) at η = 0.2 V].

As there is always some degree of uncertainty in linearization of Tafel slope and finding i°, therefore, an additional, current density at 0.2 V was introduced which clarifies all ambiguities about the exact performance of catalyst. For good activity, it is obvious for electrocatalysts to have lower η_{10}, higher i°, and higher [142]. All the parameters which determine the activity and performance of the catalysts are mentioned in Table 1 of which the best performance for HER was shown (figure 10) by newly formed hydrothermally synthesized hybrids of MoS_2 and spent catalyst.

Table 1 Electrode activity demonstrated using different parameters for HER activity of catalysts where η_{10} and η_{25} are overpotentials @ 10 mA cm^{-2} and 25 mA cm^{-2} while $i_{\circ}$ and are exchange current density and current density at 200 mV, respectively.

Catalyst	**Onset Potential (mV)**	**η_{10} (mV)**	**Tafel Slope ($mVdec^{-1}$)**	**$i_{\circ}$ ($mAcm^{-2}$)**	**$i_{0.2}$ ($mAcm^{-2}$)**	**η_{25} (mV)**
GC	180	302	255	1.42	2.2	341
CNF	201	297	145	1.90	2.6	337
MoS_2@GC	30.8	165	107	1.91	14.1	207
MoS_2@CNF	20.6	144	99	2.35	23.4	186

The hybrids exhibited an ample increase in activity with η_{10}= 0.144V, $i_{0.2}$ = 10.63 mA/cm^2, i° = 2.35 mA/cm^2 for MoS_2@CNF and η_{10}=0.165V, $i_{0.2}$ = 6.733 mA/cm^2, i° = 1.91 mA/cm^2 for MoS_2@GC, respectively. One of the crucial parameter mentioned above that aids in elucidating the HER mechanism is Tafel slope. In the Tafel slopes (figure 11), a distinct difference before and after deposition of MoS_2 was observed. From GC (255 mV dec^{-1}) to MoS_2@GC (107 mV dec^{-1}) and from CNF (145 mV dec^{-1}) to MoS_2@CNF (99 mV dec^{-1}) a major shift of about (148 mV dec^{-1}) and (46 mV dec^{-1}) was observed, respectively. From the range of Tafel slopes the mechanism with which HER proceeds can be explained. Generally, HER is described either by Hydronium ion reduction or water reduction.

(Volmer Step) $H_3O^+ + e^- + M \Longleftrightarrow M - H^* + OH^-$ *(4)*

(*Heyrovsky Step*) $H_3O^+ + e^- + M - H^* \Longleftrightarrow H_2 + OH^-$ (5)

(*Tafel Step*) $2M - H^* \Longleftrightarrow H_2 + 2M$ (6)

where the asterisk indicates the active site for HER, and H* a hydrogen atom bound to an active site. HER in alkaline aqueous media proceeds in two steps (i.e., Eq 4-6). The discharge step (Volmer reaction) is the first step and either the reaction of atom/ion (Heyrovsky reaction) or the combination of atom (Tafel reaction) is the second step [143]. Typically, the Tafel slopes, as reckoned by the classic theory, for Tafel, Heyrovsky, and Volmer reactions are around $30 mV\,dec^{-1}$, $40 mV\,dec^{-1}$, $\leq 120 mV\,dec^{-1}$, respectively [144]. Although the Tafel slope isn't an exclusive parameter for determining a specific followed mechanism but the obvious reduction in slope of MoS_2@CNF, MoS_2@GC confirms the Volmer-Heyrovsky pathway in HER kinetics [98].

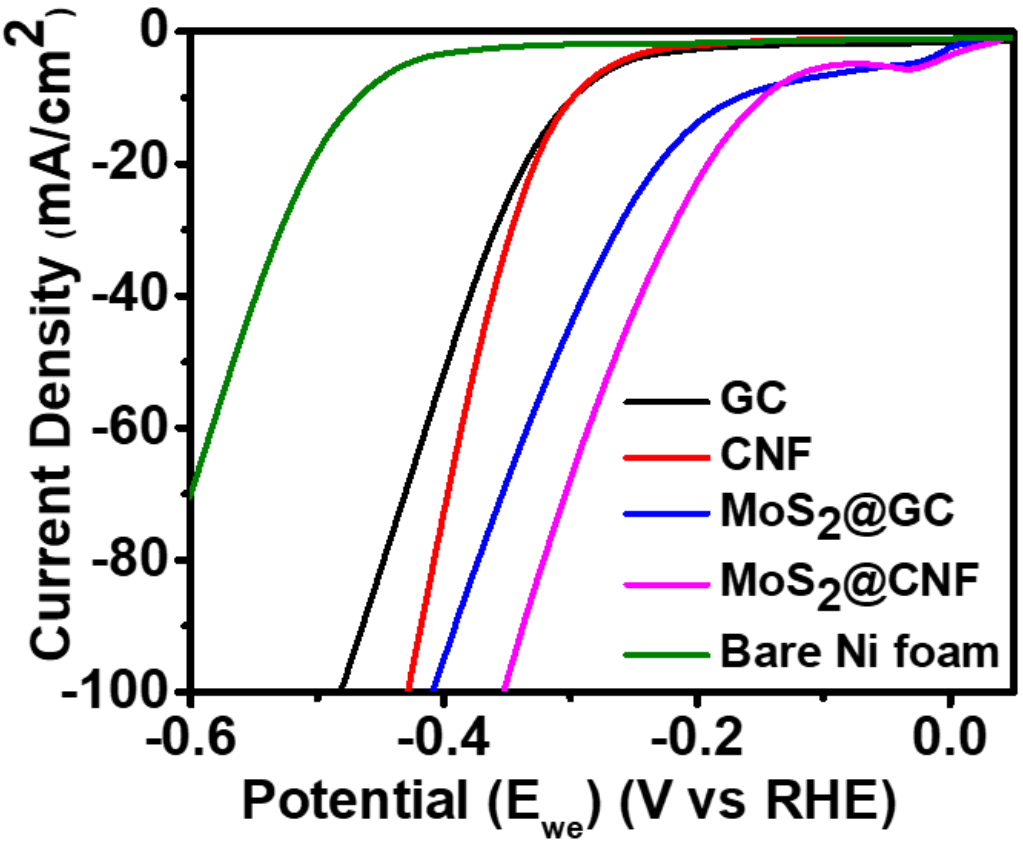

Figure 14 Linear Sweep Voltammetry of GC, CNF, MoS_2@GC, and MoS_2@CNF for HER.

The physical arguments supporting the lowest Tafel slopes, highest current densities and highest exchange current densities is that of MoS_2@CNF because the fibers and the carbon deposits in the synthesized samples provided abundant surface area, shortened the diffusion distance and provided a communicating platform for the conduction of electrons while, the deposition of MoS_2 not only enhanced the charge transfer migration but also the dissociation of water and electrostatic affinity of OH^- which improved the Volmer step and prevented the blockage of active sites by OH^- making available more empty active sites, hence, suggesting a very low activation energy for HER [145]. The comparison of overpotential to achieve a current density of 25 mA/cm^2 can be seen in the figure 16 given below.

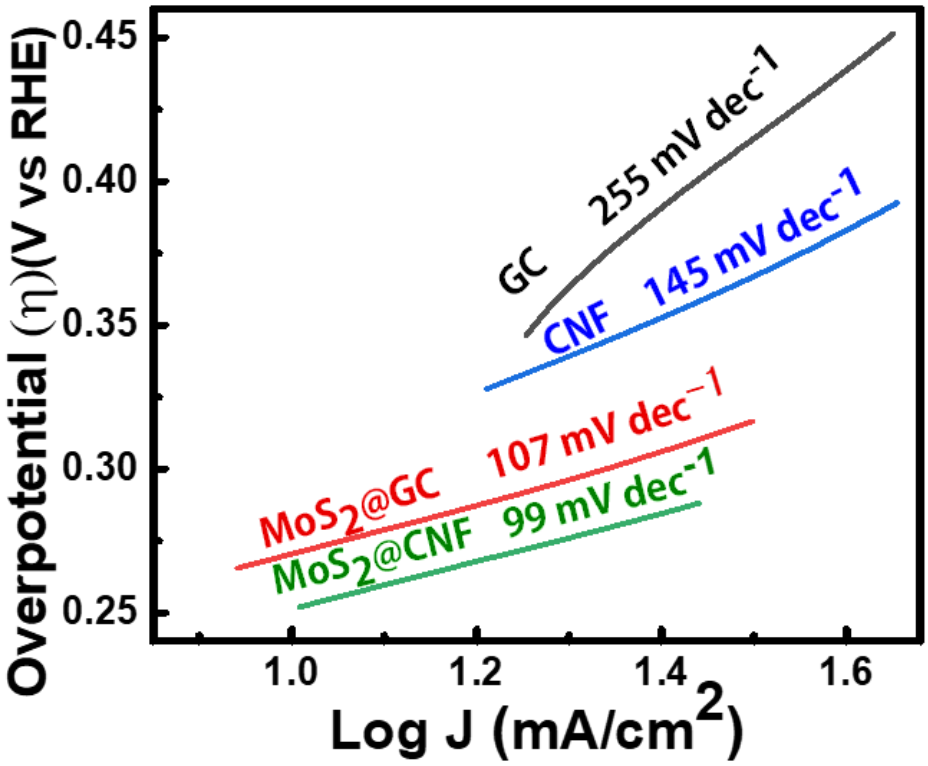

Figure 15 Tafel slopes of GC, CNF, MoS_2@GC, and MoS_2@CNF for HER.

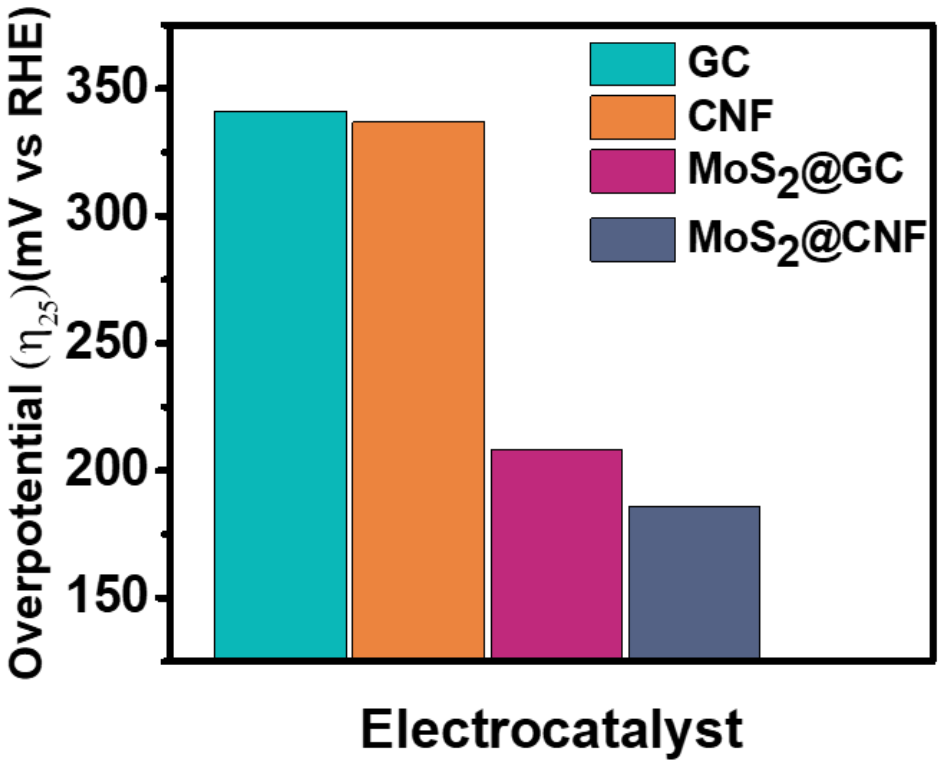

Figure 16 Overpotential comparison of GC, CNF, MoS_2@GC, and MoS_2@CNF at 25 mA/cm^2.

Due to low requirement of activation energy, a lower overpotential is required to generate a certain current density [146]. Congruently, the obtained value of η_{10} is also

low, indicating that adsorption of water on active sites is less challenging and the higher i° of MoS_2@CNF and MoS_2@GC means there is less hurdle for the flow of charges (electrons) therefore, the kinetics of HER are intrinsically fast [98]. So, it can be asserted that MoS_2 and carbon support collectively, supplemented each other in enhancing the HER activity of newly formed hybrids.

The above results shows that even by adding a small amount of MoS_2 to spent catalyst an ample increase in the activity, of about 6 folds in case of GC and about 5 folds in case of CNF can be obtained. Thence, from the obtained enhanced performance (as can be seen in the figure 13) it can be foreseen that utilization of spent catalysts and its hybridization with other dichalcogenides have a greater capacity for further improvements to achieve a cleaner and carbon-free world of electrocatalyst with a cut in cost for new efficient catalyst.

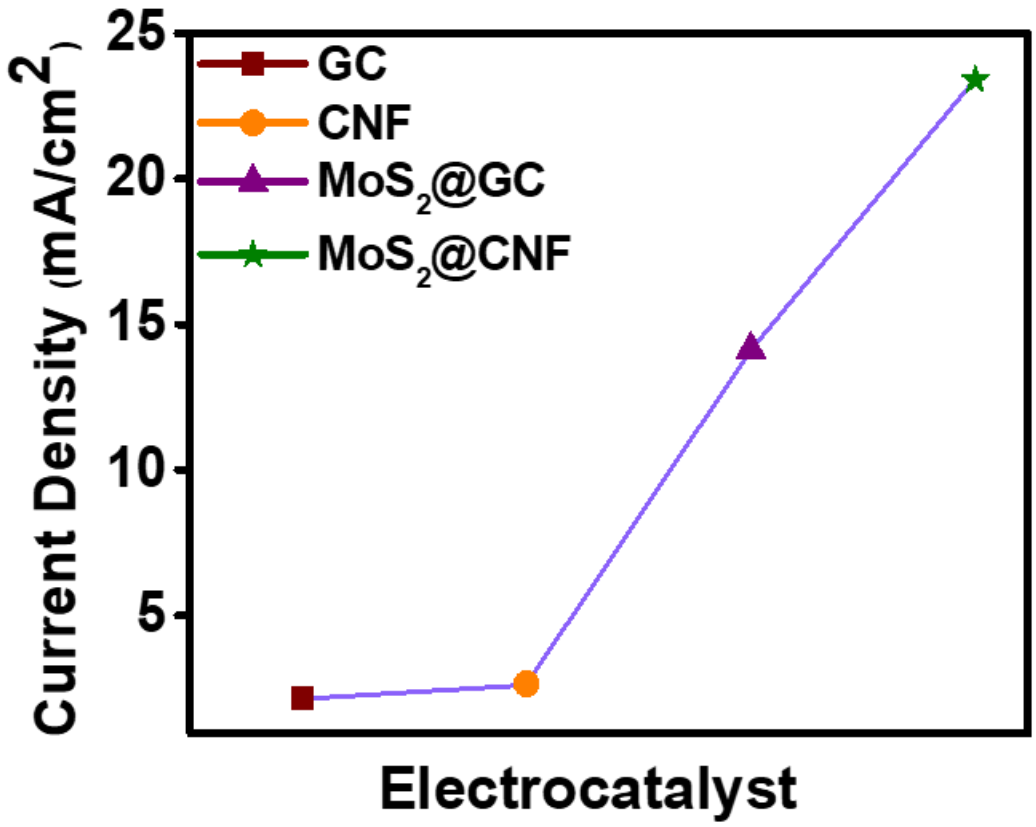

Figure 17 Current densities of GC, CNF, MoS_2@GC, and MoS_2@CNF at 200mV

5.2.2 Oxygen evolution reaction

The electrocatalytic performance of spent catalyst and the newly formed hybrids was evaluated for OER in aqueous solution of 1.0M KOH using three electrode setup. The electrocatalytic activity of spent catalysts i.e., GC and CNF and of newly fabricated hybrids MoS_2@GC and MoS_2@CNF was evaluated through the polarization curve of

linear sweep voltammetry. The activity of newly formed hybrids was evaluated under similar conditions for OER and HER. Figure 14 exhibits the polarization curves of spent catalyst and the deposited hybrids.

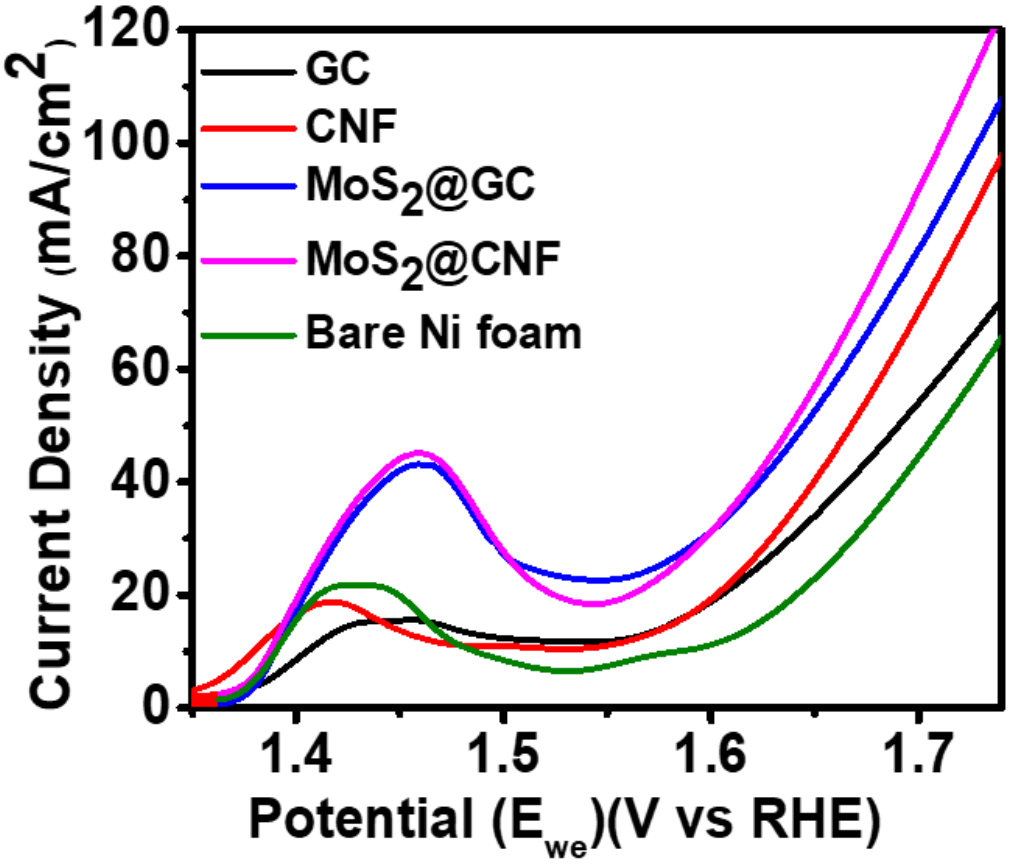

Figure 18 Linear Sweep Voltammetry of GC, CNF, MoS_2@GC, and MoS_2@CNF for OER.

In the OER polarization curves of all samples, a peak at a potential of about 1.36 V was first observed which corresponds to the oxidation of Ni foam. In the curve of MoS_2@GC a gradual increase in the current density was observed after 1.55 V while in the curve of MoS_2@CNF, after 1.54 V a sudden increase in the current density was observed. Figure 16 shows that at a current density of 25 mA cm^{-2} (figure 16). the spent catalyst i.e. GC, CNF showed an overpotential of about 309 mV and 302 mV while the fabricated catalysts i.e. MoS_2@GC and MoS_2@CNF displayed an overpotential of about 154 mV and 128 mV, respectively. At 200 mV a current density of 14.9 mA cm^{-2} for GC and 17.6 mA cm^{-2} for CNF which after depositing with MoS_2 reached to 35.7 mA cm^{-2} and 37.8 mA cm^{-2}(figure 17) for MoS_2@GC and MoS_2@CNF, respectively.

Table 2 Electrode activity demonstrated using different parameters for OER activity of catalysts where η_{25} is overpotentials @ 25 mA cm^{-2} while $i_\circ$ and $i_{0.2}$ exchange current density and current density at 200 mV, respectively.

Catalyst	**Tafel Slope ($mVdec^{-1}$)**	***i*∘ ($mAcm^{-2}$)**	***$i_{0.2}$*** **($mAcm^{-2}$)**	***η_{25}*** **(mV)**
GC	195	0.385	14.9	309
CNF	148	1.35	17.6	302
MoS_2@GC	71	1.92	35.7	154
MoS_2@CNF	41	2.11	37.8	128

The kinetics of the OER were gauged by Tafel plots i.e., figure 19. The lowest Tafel slope of MoS_2@CNF (i.e., 41 mV dec^{-1}) and MoS_2GC (i.e., 71 mV dec^{-1}) as compared to CNF (i.e., 148 mV dec^{-1}) and GC (i.e.,195 mV dec^{-1}) advocates for faster kinetics of the fabricated catalysts. The graphitic carbon present on the spent catalyst decreases inter-layer stacking of MoS_2 resulting in exposed edge sites furthermore, the transport of charges via basal plane of MoS_2 is also favored [58][147]. While, in case of MoS_2CNF the electrocatalytic activity is improved due to additional surface area of the fibers, providing more vacancy for water to adsorb, dissociate, and release oxygen moreover, showing less affinity toward OH^- [147] . The highest exchange current density revealed byMoS_2@CNF (i.e., i° = 2.11 and MoS_2@GC (i.e., i° = 1.92mA/cm^2) when compared to that of CNF (i° = 1.35mA/cm^2) and GC (i° = 0.385mA/cm^2), respectively, shows that the interfacial barrier for charge transfer is decreased due to which the kinetics of OER are significantly improved.

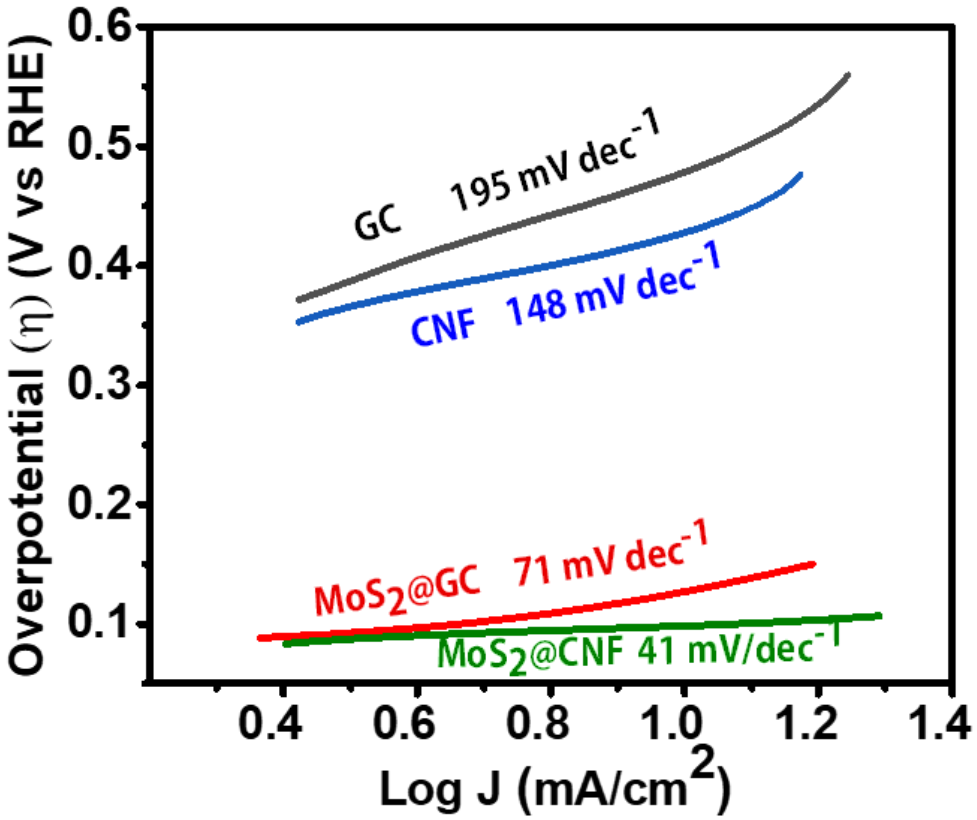

Figure 19 Tafel slopes of GC, CNF, MoS_2@GC, and MoS_2@CNF

The oxygen evolution reaction (OER) is known as a 2 or 4 electron step and the reaction mechanism is complicated. Assuming a single-site mechanism we considered the following mechanism under alkaline conditions:

$$M + OH^- \longrightarrow MOH^- \quad (7)$$

$$MOH + OH^- \longrightarrow MO + H_2O_{(l)} \quad (8)$$

$$2MO \longrightarrow 2M + O_{2\,(g)} \quad (9)$$

$$MO + OH^- \longrightarrow MOOH + e^- \quad (10)$$

$$MOOH + OH^- \longrightarrow M + O_{2\,(g)} + H_2O_{(l)} \quad (11)$$

where M denotes a site on the surface or the surface of the electrocatalyst. As the Tafel slope is below 120mV dec^{-1} and significantly low for of newly formed hybrids, therefore, it can be asserted that the surface adsorbed species produced in the early stage

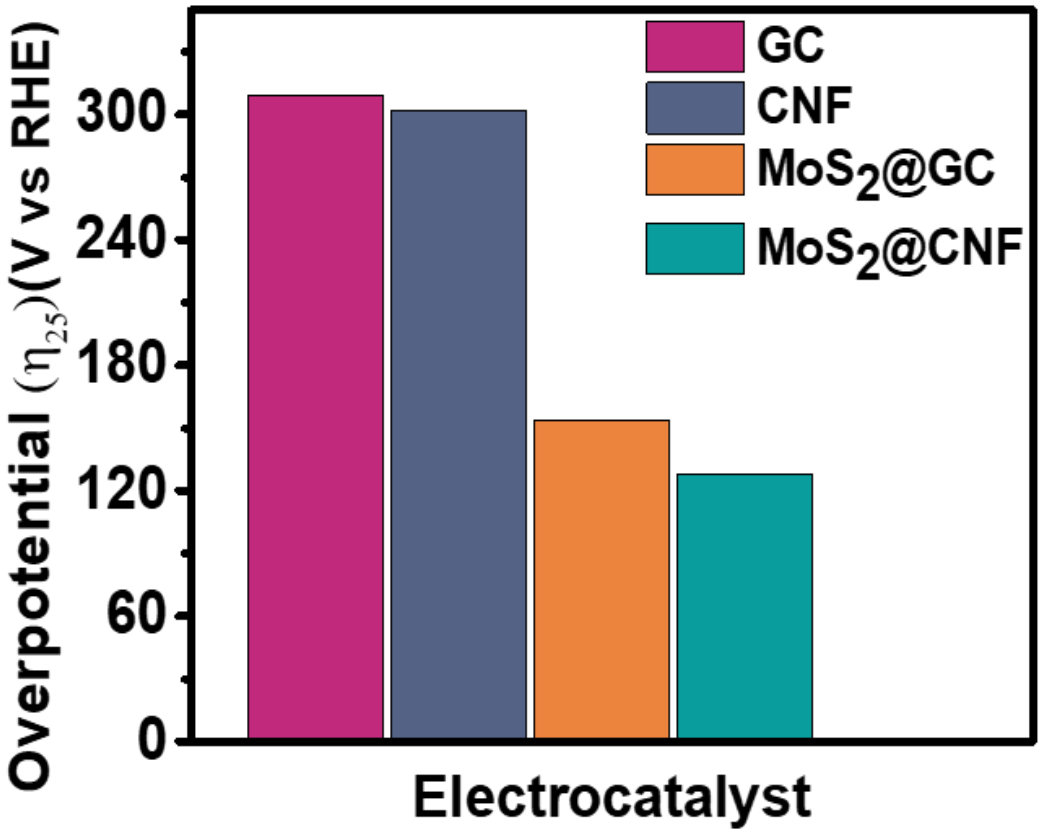

Figure 20 Overpotential comparison of spent and synthesized catalysts at 25 mA/cm^2

of OER remains predominant [148]. Furthermore, it can be stated that in the alkaline medium during the electrocatalytic process the produced OH^- likely, get attached to the active sites (S) of MoS_2@CNF and MoS_2@GC and then reacted with other dissociating OH^- to form reaction intermediates (MOH, MO and MOOH), which then on oxidation results into evolution of oxygen. The Tafel slope observed for MoS_2@CNF close to the value (40 mV dec) characteristic of a mechanism involving a pre-equilibrium consisting of a one-electron electrochemical step with a possible chemical step, followed by a one-electron electrochemical rate determining step [149]. The activity of MoS_2@CNF is the best that is reported till far because the spent catalyst also possessed Nickle atoms present at the tips of the fibers which contributed to the transportation of charges and the presence of active edges sites of the intercalated MoS_2 is another reason for delivering better electrochemical performance [50]. The comparison of greater current densities of MoS_2 can be seen in the figure below.

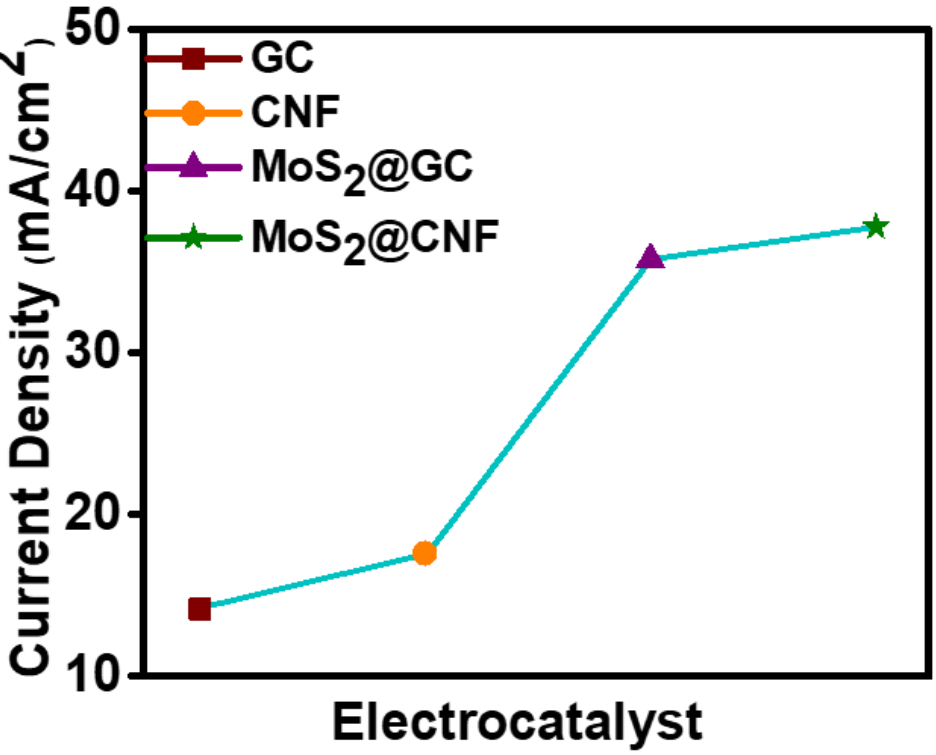

Figure 21 Current density of all samples at 200mV

5.2.3 Electrostatic Impedance Spectroscopy (EIS)

The electrostatic impedance measurements were biased to 0 V (vs. the open circuit voltage) using the three-electrode system, at a frequency ranging from 200 KHz to 100 MHz The Electrostatic impedance spectroscopy (EIS) of all the samples possesses a semicircle and then an inclined line which can be elaborated from EIS spectrum shown in figure 22 and equivalent circuit (EC).

Commonly, a simplified EC consisting of a capacitor and a resistor connected in parallel is an obvious model for carbon based materials but for complex nanohybrids the EC also changes [150,151]. In the impedance analysis for MoS_2@CNF and MoS_2@GC complications occurs in the system and a simple RC circuit is not enough to be taken as EC, therefore, with other circuit elements like R_1,R_2,C_1 and W_1, a constant phase element Q_1 (as shown in the inset of figure 7 (c)) was also introduced [152], where R_1 is the ohmic resistance caused by solution (electrolyte), R_2 is the polarization resistance , C is the faradic capacitance, Z_w ascribes to the Warburg impedance [153] while Q is a circuit component usually, used to express an imperfect capacitor in a circuit of distributed resistors and capacitors [154–156].

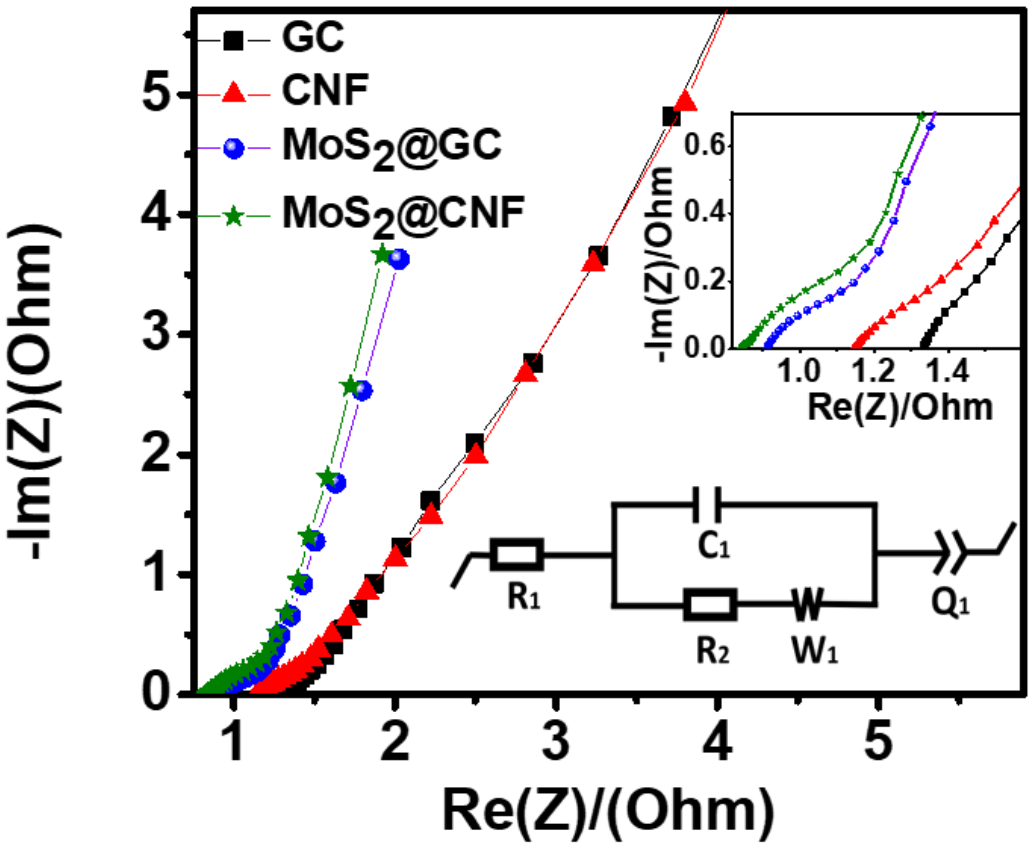

Figure 22 Nyquist plot for GC, CNF, MoS_2@CNF, and MoS_2@GC with equivalent circuit diagram.

From the Bode plot in figure 23 it can be seen that the phase angle increases with increasing frequency, which is the typical behavior of RC parallel circuit therefore, (C), R_2 and (Z_w) were modelled in parallel. In the spectrum of MoS_2@CNF and MoS_2@GC it is noted that the spike-like region is more close to the imaginary axis demonstrating fast charge-transfer kinetics and electric responses mimicking a circuit with low resistance and large capacitance connected in parallel [157]. Contrary to that, in the impedance spectrum of spent catalyst, there is visible indication of the mass diffusion obstacles for ion or charge transfer in the electrode [158]. Moreover, from Table3 and corresponding Figure7(c) it is also evident that the serial resistance (R_2) (intercept on real axis) and charge transfer resistance (diameter of the semicircle) of MoS_2@CNF and MoS_2@GC are lower than those of the spent catalyst. The serial resistance is attributed to the inter-granular electronic resistance between the active particles of material and the contact resistance between the active particles and current collector, while the charge transfer resistance (Z_w) originates at the interface of electrode/electrolyte caused by the diffusion process of ions or charge carriers, where the main charge carrier is the hydronium ion (H_3O^+) [159–161]. With good activity

and conductivity of electrocatalyst it is also requisite for electrocatalyst to be stable for which purpose stability tests like CV and chronopotentiometry (CP) is done.

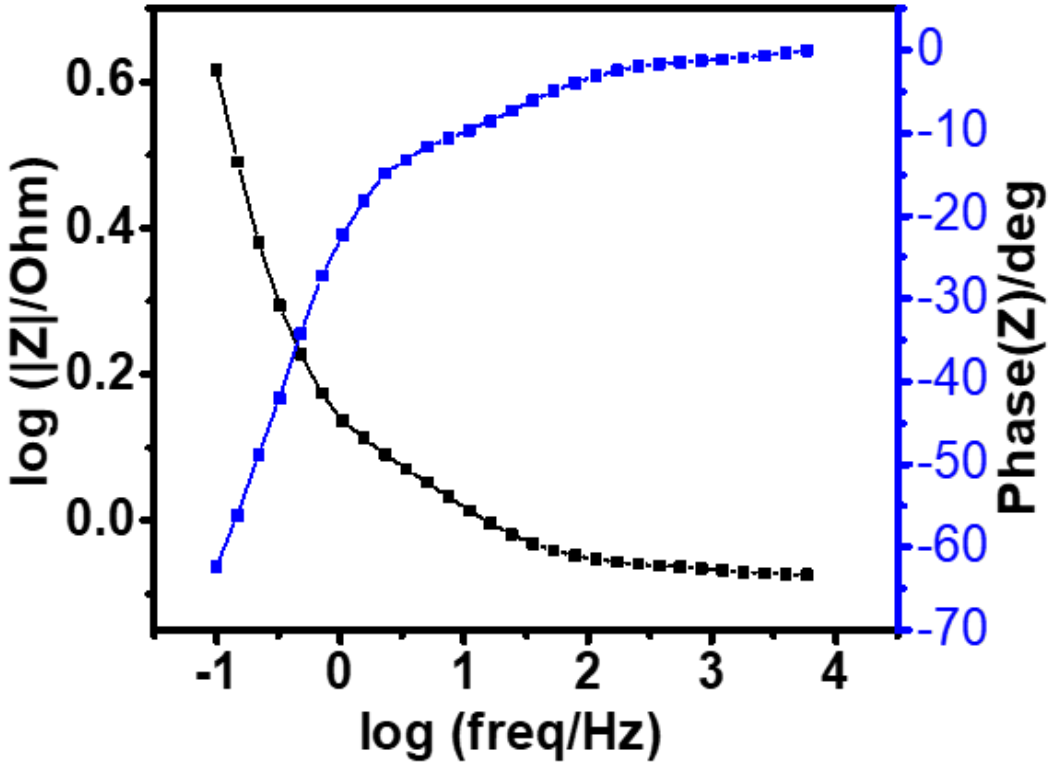

Figure 23 BODE plot for the newly synthesized sample of MoS_2@CNF.

Table 3 Electrostatic impedance spectroscopy of all samples

Catalyst	**$R_1(\Omega)$**	**$C_1(F)$**	**$R_2(\Omega)$**	**Q_1 [F.s(a−1)]**
GC	0.881	0.640	63.11	0.421
CNF	1.341	0.492	50.15	0.198
MoS_2@GC	0.946	0.621	0.627	0.928
MoS_2@CNF	0.838	0.570	8×10^{-4}	0.931

5.2.4 Cyclic Voltammetry

The comparative cyclic voltammogram of CNF, GC, MoS_2CNF, and MoS_2GC are shown in figure 24. In the potential range of -0.4 to -0.6 V at different scan rates ranging from 10 mVs^{-1} to 50 mVs^{-1} were applied for assessing the performance of spent and fabricated catalyst.

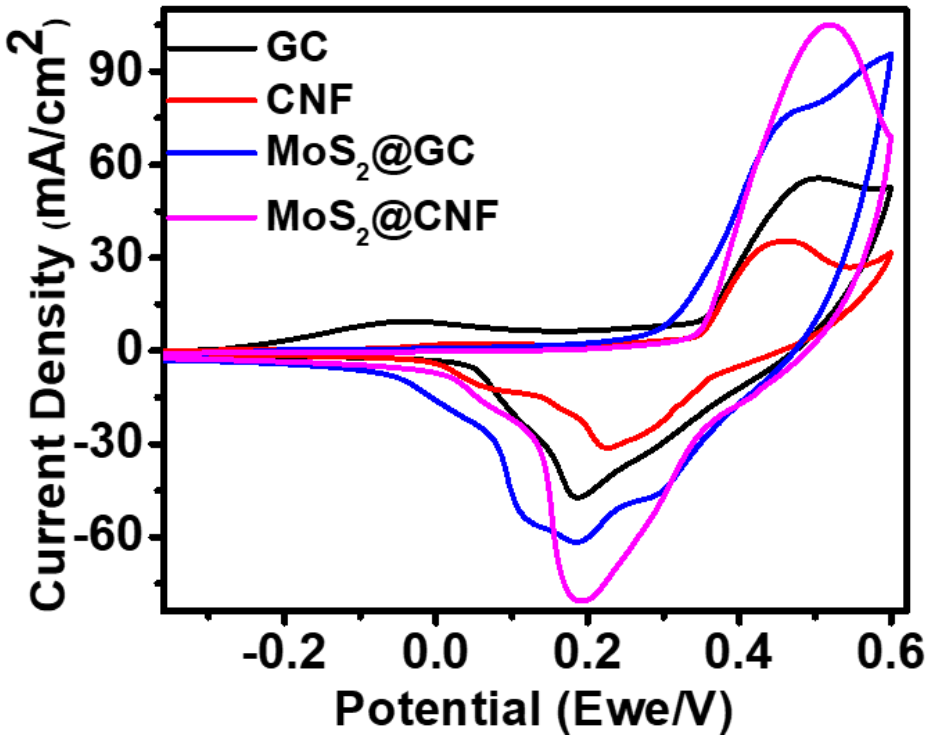

Figure 24 Cyclic voltammetry (CV) curve of spent GC, CNF, and synthesized catalyst i.e., MoS_2@GC MoS_2@CNF.

In the profile of MoS_2CNF and MoS_2GC a pair of prominent, enhanced and widely separated red-ox peaks i.e. anodic (0.493 V) and cathodic (0.2 V) peaks, associated with reduction and oxidation of the metal centers involved in charge storage is a

corroboration for typical form of red-ox system corresponding to the generation of in-situ efficient active sites for OER and HER [120,162]. When closely analyzed the CV of GC and CNF and MoS_2@CNF, the redox system bears the qualities of a typical form of electroactive charge storage devices (batteries), where the mechanism involves reversible Faradaic reactions with charge transfer and also that of pseudo-capacitor, where the mechanism involves the adsorption of electroactive ions onto the surface or near-surface region of electrode materials [163,164].This kind of duality is a specialty of carbon fibers [165], graphene [166,167] or any carbon based material [168,169] that are already in use as super-capacitors as well as psuedocapacitors where TMDs (specially MoS_2 [170–172],S_2V [173]) and oxides (like RuO_2 [174,175] and MnO_2 [176,177]) were also declared as good charge storage materials. The enhancement in the activity of GC when deposited with MoS_2 can be seen in the comparison shown in figure 24.

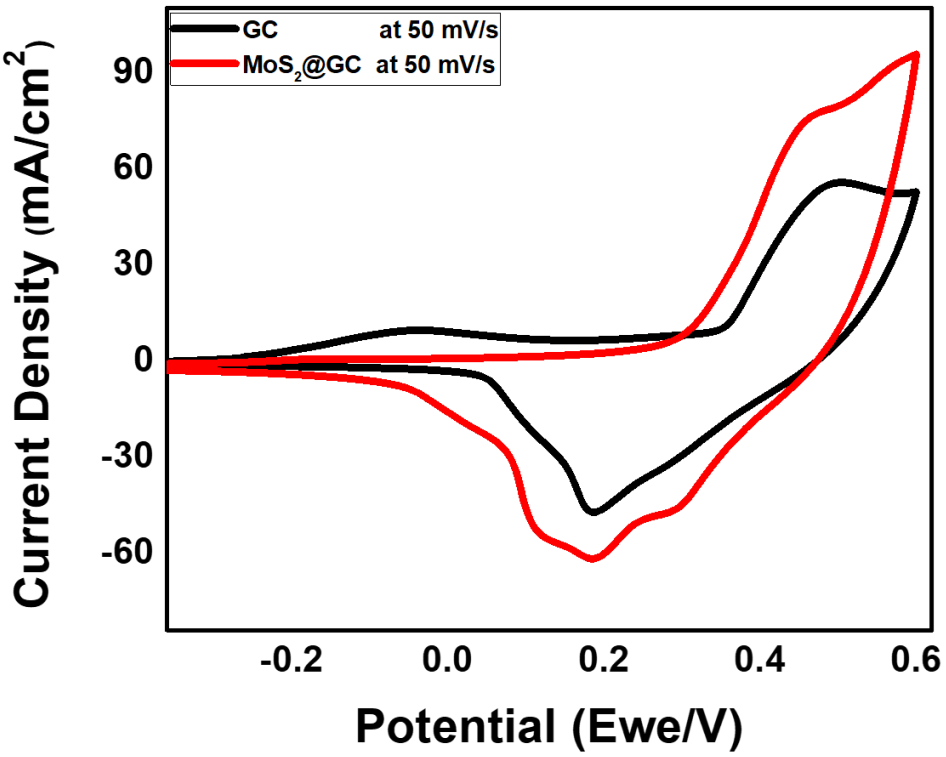

Figure 25 Comparison of cyclic voltametric curves of GC before and after deposition of MoS_2

Congruently, the improvement in the performance of spent catalyst after the addition of MoS_2 is due to the synergistic interfacial interaction between MoS_2 and carbon which dispenses an effective migration of charge carriers from the layered edges of MoS_2 to the carbon support hence, contributing to increase in current density

of about 3-4 times by MoS_2@GC as can be seen in the figure 25 while of about 2 folds by MoS_2@CNF can be seen in figure 6, respectively[178,179].

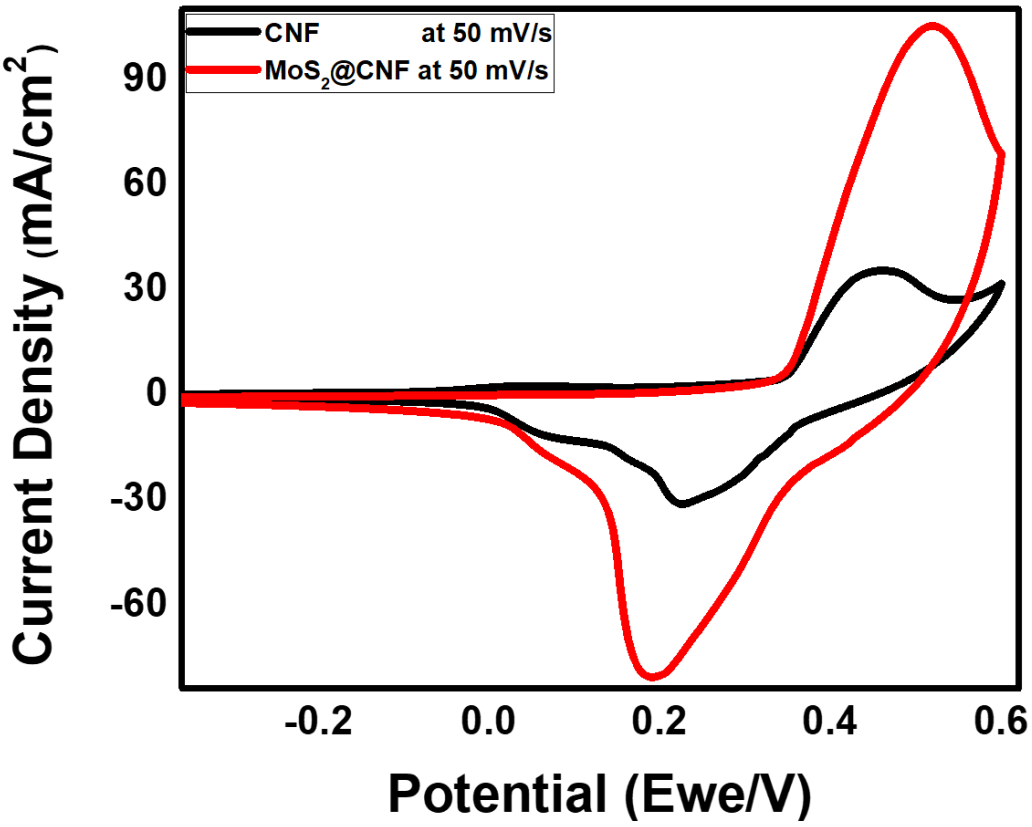

Figure 26 Comparison of cyclic voltammetry curve before and after deposition of MoS_2

Therefore, MoS_2@CNF, and MoS_2@GC exhibit the widest CV curve with highest re-dox peaks thus, showing strongest electrochemical behavior as compared to CNF, GC. Moreover, increasing scan rates accordingly increases the current response and the peak position slightly changes but the shape of CV curves retains, which indicates a good electrochemical stability and rate performance of the MoS_2@CNF and MoS_2@GC.

5.2.5 Stability Test

Long-term stability test which is crucial for determining the effectiveness of electrocatalyst in the long-run and for commercializing it for production of oxygen and hydrogen fuel using renewable energy. The stability of MoS_2@CNF and MoS_2@GC was measured by exposing these electrocatalysts to CP in the same alkaline solution

at 100 μA for 18h. A stable behavior as shown figure 27 is displayed by MoS_2@CNF and MoS_2@GC which is primarily due to their stable structural characteristics.

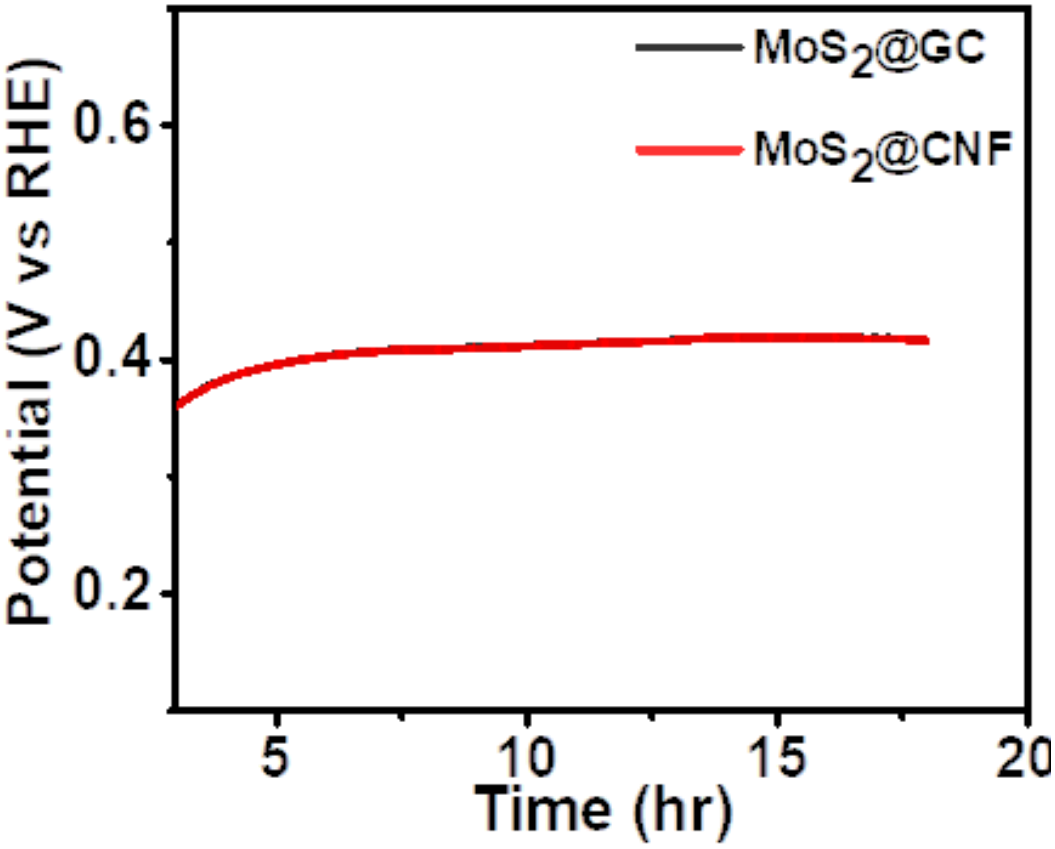

Figure 27 Chronopotentiometry (CP) of MoS_2@GC and MoS_2CNF

Due to large interfacial interaction between electrolyte and electrode leading there is low ion diffusion resistance which helps in quick ion penetration across the widely exposed active sites. Initially, the response of potential is rapid, but no prominent changes can be seen after the 3^{rd} h. The probable reason for the change is the activation of synthesized material during CP which effect can be visible in the form of rapid potential response [180].

The LSV polarization curve in figure 28 for HER was obtained after performing CV and CP which clearly is a testimonial for the stability of newly formed hybrids. While a clear effect of scan rate on the current density of MoS_2@CNF is displayed in figure 29. As a good OER catalyst may not be a good HER catalyst due to different rate determining steps for respective reactions which also limits the Butler-Volmer equation to describing chemically reversible electrocatalytic reactions [148]. But our catalysts have performed for HER as well as for OER.

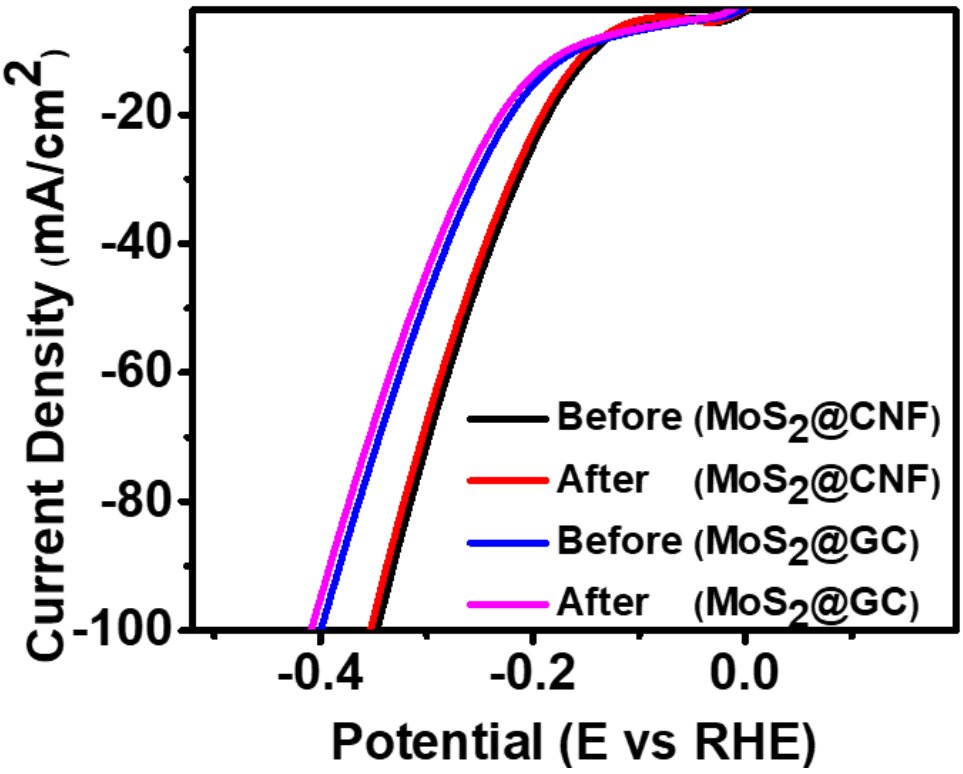

Figure 28 Linear sweep voltammetry (LSV) of MoS_2@GC and MoS_2@CNF after long term stability tests.

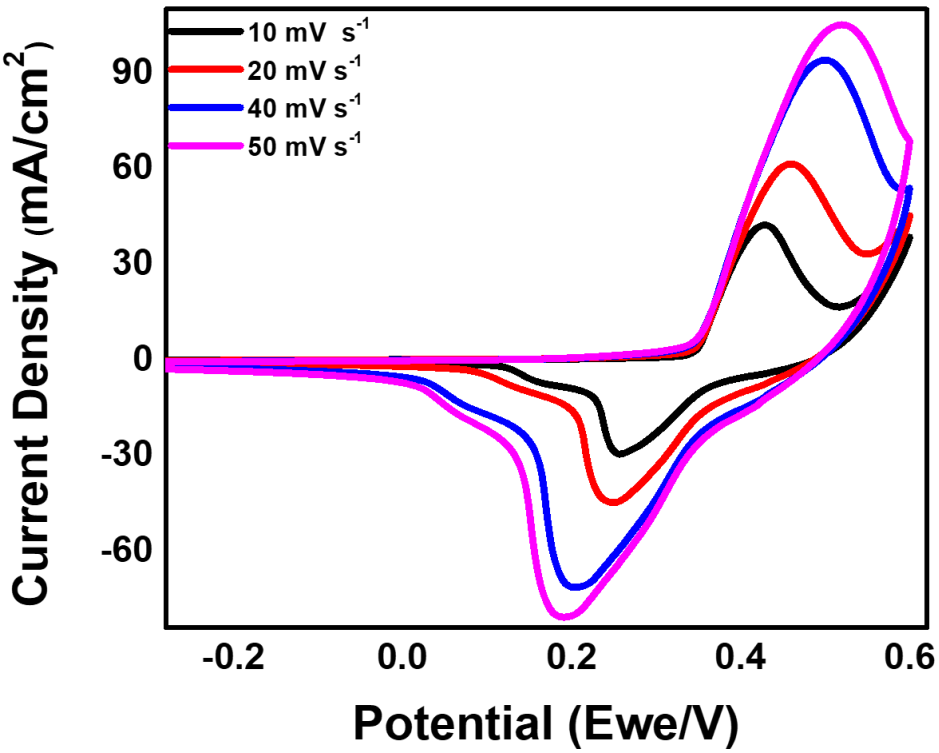

Figure 29 Cyclic voltammetry curve for MoS_2@CNF at different scan rates.

Conclusions

Electrochemical water splitting is contemplated to be an effective solution to overcome energy crises and adverse environmental challenges. Many approaches have been carried out to build an economical potent electrocatalyst. So, we synthesized catalysts consisting of spent methane reforming catalyst by insitu deposition of MoS_2 through a minimalistic and cost-effective hydrothermal method. The successful formation of MoS_2@CNF and MoS_2@GC was confirmed by morphological and analytical characterization techniques, after assurance, these fabricated catalysts were tested for electrochemical HER and OER performances. The evaluation of electrochemical performance of showed lowest Tafel slopes, highest $i^{\circ}_{0.2}$ and low η_{25} for OER and HER indicated that the adsorption of OER and HER intermediates in MoS_2@CNF and MoS_2@GC catalysts was synergistically enhanced due to coupling of MoS_2 and spent catalyst, meanwhile, the carbon present on the spent catalyst not only provided mechanical support for MoS_2 but also facilitated the electron transfer between MoS_2 and the alkaline solution. This work provided a promising demonstration of utilizing spent deactivated catalyst for electrochemical applications moreover, it also gives a clear way forward for using carbon-deactivated catalysts with the addition of very minimal amount of low cost HER/OER catalyst for achieving accelerated overall water splitting.

References

[1] Robert Boyle, Richard Davis London. 1 (1672) 438.

[2] H. Cavendish, Philos. Trans. R. Soc. London. 10 (1766) 141–184.

[3] A. Züttel, L. Schlapbach, A. Borgschulte, Hydrog. as a Futur. Energy Carr. 2 (2008) 7–20.

[4] Jose M Bermudez, T. Hasegawa, Hydrogen, 14 (2020) 33.

[5] M. Williams, Universe Today 5. (2016) 15.

[6] N. MURADOV, T. VEZIROLU, Int. J. Hydrogen Energy. 30 (2005) 225–237.

[7] H.-O.P. Mbow, A. Reisinger, J. Canadell, P. O'Brien, Inter Gov. Panel Clim. Chang. 1 (2017) 32.

[8] J.M. Ogden, M.M. Steinbugler, T.G. Kreutz, J. Power Sources. 79 (1999) 143–168.

[9] M. ONOZAKI, K. WATANABE, T. HASHIMOTO, H. SAEGUSA, Y. KATAYAMA, Fuel. 85 (2006) 143–149.

[10] C. Song, Catal. Today. 77 (2002) 17–49.

[11] R. Farrauto, S. Hwang, L. Shore, W. Ruettinger, J. Lampert, T. Giroux, Y. Liu, O. Ilinich, Annu. Rev. Mater. Res. 33 (2003) 1–27.

[12] K. LIN, S. CHOWDHURY, C. SHEN, C. YEH, Catal. Today. 136 (2008) 281–290.

[13] A.M. Adris, B.B. Pruden, C.J. Lim, J.R. Grace, Can. J. Chem. Eng. 74 (1996) 177–186.

[14] Y. Shirasaki, T. Tsuneki, Y. Ota, I. Yasuda, S. Tachibana, H. Nakajima, K. Kobayashi, Int. J. Hydrogen Energy. 34 (2009) 4482–4487.

[15] M. Bui, C.S. Adjiman, A. Bardow, E.J. Anthony, A. Boston, S. Brown, P.S. Fennell, S. Fuss, A. Galindo, L.A. Hackett, others, Energy \& Environ. Sci. 11 (2018) 1062–1176.

[16] I.E. Agency, CO2 Capture and Storage: A Key Carbon Abatement Option,

2008.

[17] IEA, (2020) 203.

[18] M. Marafi, A. Stanislaus, Resour. Conserv. Recycl. 53 (2008) 1–26.

[19] A. Ochoa, J. Bilbao, A.G. Gayubo, P. Castaño, Renew. Sustain. Energy Rev. 119 (2020) 109600.

[20] P. Dufresne, Appl. Catal. A Gen. 322 (2007) 67–75.

[21] J.W. Han, J.S. Park, M.S. Choi, H. Lee, Appl. Catal. B Environ. 203 (2017) 625–632.

[22] A. KONIECZNY, K. MONDAL, T. WILTOWSKI, P. DYDO, Int. J. Hydrogen Energy. 33 (2008) 264–272.

[23] S. GRIGORIEV, V. POREMBSKY, V. FATEEV, Int. J. Hydrogen Energy. 31 (2006) 171–175.

[24] J. Pettersson, B. Ramsey, D. Harrison, J. Power Sources. 157 (2006) 28–34.

[25] J. Turner, G. Sverdrup, M.K. Mann, P.-C. Maness, B. Kroposki, M. Ghirardi, R.J. Evans, D. Blake, Int. J. Energy Res. 32 (2008) 379–407.

[26] C.N. Hamelinck, A.P.. Faaij, J. Power Sources. 111 (2002) 1–22.

[27] S.-E. Lindquist, C. Fell, FUELS – HYDROGEN PRODUCTION | Photoelectrolysis, in: Encycl. Electrochem. Power Sources, Elsevier, 2009: pp. 369–383.

[28] J. E. Funk, Int. J. Hydrogen Energy. 26 (2001) 185–190.

[29] A. Steinfeld, Sol. Energy. 78 (2005) 603–615.

[30] J.K. Basco, M.A. Lewis, M. Serban, Hydrogen Production at <550°C Using a Low Temperature Thermochemical Cycle, in: 2004: pp. 145–156.

[31] O. Diaz-Morales, F. Calle-Vallejo, C. de Munck, M.T.M. Koper, Chem. Sci. 4 (2013) 2334.

[32] X. Zou, Y. Zhang, Chem. Soc. Rev. 44 (2015) 5148–5180.

[33] A. Lasia, Hydrogen evolution reaction, in: Handb. Fuel Cells, John Wiley &

Sons, Ltd, Chichester, UK, 2010.

[34] J. HORIUTI, A. MATSUDA, M. ENYO, H. KITA, THE MECHANISM OF THE HYDROGEN EVOLUTION REACTION, in: Electrochemistry, Elsevier, 1965: pp. 750–779.

[35] C.G. Morales-Guio, L.-A. Stern, X. Hu, Chem. Soc. Rev. 43 (2014) 6555.

[36] R.B. Levy, M. Boudart, Science (80-.). 181 (1973) 547–549.

[37] J. Zhu, L. Hu, P. Zhao, L.Y.S. Lee, K.-Y. Wong, Chem. Rev. 120 (2020) 851–918.

[38] F. Lv, J. Feng, K. Wang, Z. Dou, W. Zhang, J. Zhou, C. Yang, M. Luo, Y. Yang, Y. Li, others, ACS Cent. Sci. 4 (2018) 1244–1252.

[39] Y. Lee, J. Suntivich, K.J. May, E.E. Perry, Y. Shao-Horn, J. Phys. Chem. Lett. 3 (2012) 399–404.

[40] P. Wang, X. Zhang, J. Zhang, S. Wan, S. Guo, G. Lu, J. Yao, X. Huang, Nat. Commun. 8 (2017) 1–9.

[41] S. Park, Y. Shao, J. Liu, Y. Wang, Energy \& Environ. Sci. 5 (2012) 9331–9344.

[42] J.N. Tiwari, S. Sultan, C.W. Myung, T. Yoon, N. Li, M. Ha, A.M. Harzandi, H.J. Park, D.Y. Kim, S.S. Chandrasekaran, others, Nat. Energy. 3 (2018) 773–782.

[43] C.C.L. McCrory, S. Jung, I.M. Ferrer, S.M. Chatman, J.C. Peters, T.F. Jaramillo, J. Am. Chem. Soc. 137 (2015) 4347–4357.

[44] X. Xia, L. Wang, N. Sui, V.L. Colvin, W.Y. William, Nanoscale. 12 (2020) 12249–12262.

[45] J. Yin, J. Jin, H. Lin, Z. Yin, J. Li, M. Lu, L. Guo, P. Xi, Y. Tang, C.-H. Yan, Adv. Sci. 7 (2020) 1903070.

[46] M. Liao, Q. Zhang, W.H.E. Schwarz, Inorg. Chem. 34 (1995) 5597–5605.

[47] B. Hinnemann, P.G. Moses, J. Bonde, K.P. Jørgensen, J.H. Nielsen, S. Horch, I. Chorkendorff, J.K. Nørskov, J. Am. Chem. Soc. 127 (2005) 5308–5309.

[48] T.F. Jaramillo, K.P. Jorgensen, J. Bonde, J.H. Nielsen, S. Horch, I.

Chorkendorff, Science (80-.). 317 (2007) 100–102.

[49] L. Li, Z. Qin, L. Ries, S. Hong, T. Michel, J. Yang, C. Salameh, M. Bechelany, P. Miele, D. Kaplan, others, ACS Nano. 13 (2019) 6824–6834.

[50] J. Wu, M. Liu, K. Chatterjee, K.P. Hackenberg, J. Shen, X. Zou, Y. Yan, J. Gu, Y. Yang, J. Lou, P.M. Ajayan, Adv. Mater. Interfaces. 3 (2016) 1500669.

[51] R. Khatri, N.K. Puri, Vacuum. 175 (2020) 109250.

[52] M. Acerce, D. Voiry, M. Chhowalla, Nat. Nanotechnol. 10 (2015) 313–318.

[53] Y.-C. Lin, D.O. Dumcenco, Y.-S. Huang, K. Suenaga, Nat. Nanotechnol. 9 (2014) 391–396.

[54] W. Ma, H. Li, S. Jiang, G. Han, J. Gao, X. Yu, H. Lian, W. Tu, Y. Han, R. Ma, ACS Sustain. Chem. \& Eng. 6 (2018) 14441–14449.

[55] W. Li, Z. Zhang, W. Zhang, S. Zou, ACS Omegaf. 2 (2017) 5087–5094.

[56] Y.M. Chen, X.Y. Yu, Z. Li, U. Paik, X.W.D. Lou, Sci. Adv. 2 (2016) e1600021.

[57] X. Hou, H. Zhou, M. Zhao, Y. Cai, Q. Wei, ACS Sustain. Chem. \& Eng. 8 (2020) 5724–5733.

[58] X. Xiong, W. Luo, X. Hu, C. Chen, L. Qie, D. Hou, Y. Huang, Sci. Rep. 5 (2015) 1–6.

[59] J. Kibsgaard, Z. Chen, B.N. Reinecke, T.F. Jaramillo, Nat. Mater. 11 (2012) 963–969.

[60] Y. Wan, Z. Zhang, X. Xu, Z. Zhang, P. Li, X. Fang, K. Zhang, K. Yuan, K. Liu, G. Ran, Y. Li, Y. Ye, L. Dai, Nano Energy. 51 (2018) 786–792.

[61] D. Kong, H. Wang, J.J. Cha, M. Pasta, K.J. Koski, J. Yao, Y. Cui, Nano Lett. 13 (2013) 1341–1347.

[62] L. Yang, H. Hong, Q. Fu, Y. Huang, J. Zhang, X. Cui, Z. Fan, K. Liu, B. Xiang, ACS Nano. 9 (2015) 6478–6483.

[63] J. Hu, B. Huang, C. Zhang, Z. Wang, Y. An, D. Zhou, H. Lin, M.K.H. Leung, S. Yang, Energy Environ. Sci. 10 (2017) 593–603.

[64] Y. Tan, P. Liu, L. Chen, W. Cong, Y. Ito, J. Han, X. Guo, Z. Tang, T. Fujita, A. Hirata, M.W. Chen, Adv. Mater. 26 (2014) 8023–8028.

[65] J. Deng, H. Li, J. Xiao, Y. Tu, D. Deng, H. Yang, H. Tian, J. Li, P. Ren, X. Bao, Energy Environ. Sci. 8 (2015) 1594–1601.

[66] H. Li, C. Tsai, A.L. Koh, L. Cai, A.W. Contryman, A.H. Fragapane, J. Zhao, H.S. Han, H.C. Manoharan, F. Abild-Pedersen, J.K. Nørskov, X. Zheng, Nat. Mater. 15 (2016) 48–53.

[67] J. Xie, H. Zhang, S. Li, R. Wang, X. Sun, M. Zhou, J. Zhou, X.W.D. Lou, Y. Xie, Adv. Mater. 25 (2013) 5807–5813.

[68] Y. Guo, X. Zhang, X. Zhang, T. You, J. Mater. Chem. A. 3 (2015) 15927–15934.

[69] J. Zhang, Y. Wang, J. Cui, J. Wu, Y. Li, T. Zhu, H. Kang, J. Yang, J. Sun, Y. Qin, Y. Zhang, P.M. Ajayan, Y. Wu, J. Phys. Chem. Lett. 10 (2019) 3282–3289.

[70] Y. Yin, J. Han, Y. Zhang, X. Zhang, P. Xu, Q. Yuan, L. Samad, X. Wang, Y. Wang, Z. Zhang, P. Zhang, X. Cao, B. Song, S. Jin, J. Am. Chem. Soc. 138 (2016) 7965–7972.

[71] Y. Xu, L. Wang, X. Liu, S. Zhang, C. Liu, D. Yan, Y. Zeng, Y. Pei, Y. Liu, S. Luo, J. Mater. Chem. A. 4 (2016) 16524–16530.

[72] H. Li, M. Du, M.J. Mleczko, A.L. Koh, Y. Nishi, E. Pop, A.J. Bard, X. Zheng, J. Am. Chem. Soc. 138 (2016) 5123–5129.

[73] C. Tsai, H. Li, S. Park, J. Park, H.S. Han, J.K. Nørskov, X. Zheng, F. Abild-Pedersen, Nat. Commun. 8 (2017) 15113.

[74] Q. Xu, Y. Liu, H. Jiang, Y. Hu, H. Liu, C. Li, Adv. Energy Mater. 9 (2019) 1802553.

[75] Z. Ji, C. Trickett, X. Pei, O.M. Yaghi, J. Am. Chem. Soc. 140 (2018) 13618–13622.

[76] J. Bonde, P.G. Moses, T.F. Jaramillo, J.K. Nørskov, I. Chorkendorff, Faraday Discuss. 140 (2009) 219–231.

[77] Z. Chen, K. Leng, X. Zhao, S. Malkhandi, W. Tang, B. Tian, L. Dong, L. Zheng,

M. Lin, B.S. Yeo, K.P. Loh, Nat. Commun. 8 (2017) 14548.

[78] K. Qi, S. Yu, Q. Wang, W. Zhang, J. Fan, W. Zheng, X. Cui, J. Mater. Chem. A. 4 (2016) 4025–4031.

[79] B.B. Li, S.Z. Qiao, X.R. Zheng, X.J. Yang, Z.D. Cui, S.L. Zhu, Z.Y. Li, Y.Q. Liang, J. Power Sources. 284 (2015) 68–76.

[80] X. Sun, J. Dai, Y. Guo, C. Wu, F. Hu, J. Zhao, X. Zeng, Y. Xie, Nanoscale. 6 (2014) 8359–8367.

[81] H. Wang, Z. Lu, S. Xu, D. Kong, J.J. Cha, G. Zheng, P.-C. Hsu, K. Yan, D. Bradshaw, F.B. Prinz, Y. Cui, Proc. Natl. Acad. Sci. 110 (2013) 19701–19706.

[82] K. Zhang, H.-J. Kim, J.-T. Lee, G.-W. Chang, X. Shi, W. Kim, M. Ma, K. Kong, J.-M. Choi, M.-S. Song, J.H. Park, ChemSusChem. 7 (2014) 2489–2495.

[83] H. Wang, C. Tsai, D. Kong, K. Chan, F. Abild-Pedersen, J.K. Nørskov, Y. Cui, Nano Res. 8 (2015) 566–575.

[84] J. Zhang, T. Wang, P. Liu, S. Liu, R. Dong, X. Zhuang, M. Chen, X. Feng, Energy Environ. Sci. 9 (2016) 2789–2793.

[85] H. Li, S. Chen, X. Jia, B. Xu, H. Lin, H. Yang, L. Song, X. Wang, Nat. Commun. 8 (2017) 15377.

[86] Y. Shi, Y. Zhou, D.-R. Yang, W.-X. Xu, C. Wang, F.-B. Wang, J.-J. Xu, X.-H. Xia, H.-Y. Chen, J. Am. Chem. Soc. 139 (2017) 15479–15485.

[87] J. Xie, J. Zhang, S. Li, F. Grote, X. Zhang, H. Zhang, R. Wang, Y. Lei, B. Pan, Y. Xie, J. Am. Chem. Soc. 135 (2013) 17881–17888.

[88] J. Zhou, G. Fang, A. Pan, S. Liang, ACS Appl. Mater. Interfaces. 8 (2016) 33681–33689.

[89] D. Gao, B. Xia, C. Zhu, Y. Du, P. Xi, D. Xue, J. Ding, J. Wang, J. Mater. Chem. A. 6 (2018) 510–515.

[90] P. Liu, J. Zhu, J. Zhang, P. Xi, K. Tao, D. Gao, D. Xue, ACS Energy Lett. 2 (2017) 745–752.

[91] G. Gao, Y. Jiao, F. Ma, Y. Jiao, E. Waclawik, A. Du, J. Phys. Chem. C. 119

(2015) 13124–13128.

[92] X. Gan, L.Y.S. Lee, K. Wong, T.W. Lo, K.H. Ho, D.Y. Lei, H. Zhao, ACS Appl. Energy Mater. 1 (2018) 4754–4765.

[93] M.A. Lukowski, A.S. Daniel, F. Meng, A. Forticaux, L. Li, S. Jin, J. Am. Chem. Soc. 135 (2013) 10274–10277.

[94] Q. Tang, D. Jiang, ACS Catal. 6 (2016) 4953–4961.

[95] D. Voiry, M. Salehi, R. Silva, T. Fujita, M. Chen, T. Asefa, V.B. Shenoy, G. Eda, M. Chhowalla, Nano Lett. 13 (2013) 6222–6227.

[96] N.H. Attanayake, A.C. Thenuwara, A. Patra, Y. V. Aulin, T.M. Tran, H. Chakraborty, E. Borguet, M.L. Klein, J.P. Perdew, D.R. Strongin, ACS Energy Lett. 3 (2018) 7–13.

[97] C. Tan, Z. Luo, A. Chaturvedi, Y. Cai, Y. Du, Y. Gong, Y. Huang, Z. Lai, X. Zhang, L. Zheng, X. Qi, M.H. Goh, J. Wang, S. Han, X.-J. Wu, L. Gu, C. Kloc, H. Zhang, Adv. Mater. 30 (2018) 1705509.

[98] M.A.R. Anjum, H.Y. Jeong, M.H. Lee, H.S. Shin, J.S. Lee, Adv. Mater. 30 (2018) 1707105.

[99] E. Ha, W. Liu, L. Wang, H.-W. Man, L. Hu, S.C.E. Tsang, C.T.-L. Chan, W.-M. Kwok, L.Y.S. Lee, K.-Y. Wong, Sci. Rep. 7 (2017) 39411.

[100] W. Chen, E.J.G. Santos, W. Zhu, E. Kaxiras, Z. Zhang, Nano Lett. 13 (2013) 509–514.

[101] C. Tsai, F. Abild-Pedersen, J.K. Nørskov, Nano Lett. 14 (2014) 1381–1387.

[102] L. Liao, J. Zhu, X. Bian, L. Zhu, M.D. Scanlon, H.H. Girault, B. Liu, Adv. Funct. Mater. 23 (2013) 5326–5333.

[103] S.-K. Park, D.Y. Chung, D. Ko, Y.-E. Sung, Y. Piao, J. Mater. Chem. A. 4 (2016) 12720–12725.

[104] J. Dolinska, A. Chidambaram, W. Adamkiewicz, M. Estili, W. Lisowski, M. Iwan, B. Palys, E.J.R. Sudholter, F. Marken, M. Opallo, L. Rassaei, J. Mater. Chem. B. 4 (2016) 1448–1457.

[105] J. Ren, Y. Zhou, L. Xia, Q. Zheng, J. Liao, E. Long, F. Xie, C. Xu, D. Lin, J. Mater. Chem. A. 6 (2018) 13835–13847.

[106] B. Chen, H. Lu, J. Zhou, C. Ye, C. Shi, N. Zhao, S.-Z. Qiao, Adv. Energy Mater. 8 (2018) 1702909.

[107] X. Bian, J. Zhu, L. Liao, M.D. Scanlon, P. Ge, C. Ji, H.H. Girault, B. Liu, Electrochem. Commun. 22 (2012) 128–132.

[108] D.J. Li, U.N. Maiti, J. Lim, D.S. Choi, W.J. Lee, Y. Oh, G.Y. Lee, S.O. Kim, Nano Lett. 14 (2014) 1228–1233.

[109] D. McAteer, Z. Gholamvand, N. McEvoy, A. Harvey, E. O'Malley, G.S. Duesberg, J.N. Coleman, ACS Nano. 10 (2016) 672–683.

[110] N. Zhang, S. Gan, T. Wu, W. Ma, D. Han, L. Niu, ACS Appl. Mater. Interfaces. 7 (2015) 12193–12202.

[111] X. Zhang, Y. Zhang, B.-B. Yu, X.-L. Yin, W.-J. Jiang, Y. Jiang, J.-S. Hu, L.-J. Wan, J. Mater. Chem. A. 3 (2015) 19277–19281.

[112] Z. Xiang, Z. Zhang, X. Xu, Q. Zhang, C. Yuan, Carbon N. Y. 98 (2016) 84–89.

[113] H. Wang, Z. Lu, D. Kong, J. Sun, T.M. Hymel, Y. Cui, ACS Nano. 8 (2014) 4940–4947.

[114] A.P. Murthy, J. Theerthagiri, J. Madhavan, K. Murugan, Phys. Chem. Chem. Phys. 19 (2017) 1988–1998.

[115] Z. Chen, D. Cummins, B.N. Reinecke, E. Clark, M.K. Sunkara, T.F. Jaramillo, Nano Lett. 11 (2011) 4168–4175.

[116] Y. Rheem, Y. Han, K.H. Lee, S.-M. Choi, N. V Myung, Nanotechnology. 28 (2017) 105605.

[117] X. Huang, Z. Zeng, S. Bao, M. Wang, X. Qi, Z. Fan, H. Zhang, Nat. Commun. 4 (2013) 1444.

[118] Y. Shi, J. Wang, C. Wang, T.-T. Zhai, W.-J. Bao, J.-J. Xu, X.-H. Xia, H.-Y. Chen, J. Am. Chem. Soc. 137 (2015) 7365–7370.

[119] J. Huang, D. Hou, Y. Zhou, W. Zhou, G. Li, Z. Tang, L. Li, S. Chen, J. Mater.

Chem. A. 3 (2015) 22886–22891.

[120] Y. Yang, K. Zhang, H. Lin, X. Li, H.C. Chan, L. Yang, Q. Gao, Acs Catal. 7 (2017) 2357–2366.

[121] Y. Guo, J. Tang, H. Qian, Z. Wang, Y. Yamauchi, Chem. Mater. 29 (2017) 5566–5573.

[122] J. Zhang, T. Wang, D. Pohl, B. Rellinghaus, R. Dong, S. Liu, X. Zhuang, X. Feng, Angew. Chemie Int. Ed. 55 (2016) 6702–6707.

[123] Z. Zhao, F. Qin, S. Kasiraju, L. Xie, M.K. Alam, S. Chen, D. Wang, Z. Ren, Z. Wang, L.C. Grabow, J. Bao, ACS Catal. 7 (2017) 7312–7318.

[124] J. Jeon, Y. Park, S. Choi, J. Lee, S.S. Lim, B.H. Lee, Y.J. Song, J.H. Cho, Y.H. Jang, S. Lee, ACS Nano. 12 (2018) 338–346.

[125] S. Yang, Y. Wang, H. Zhang, Y. Zhang, L. Liu, L. Fang, X. Yang, X. Gu, Y. Wang, J. Catal. 371 (2019) 20–26.

[126] I.S. Amiinu, Z. Pu, X. Liu, K.A. Owusu, H.G.R. Monestel, F.O. Boakye, H. Zhang, S. Mu, Adv. Funct. Mater. 27 (2017) 1702300.

[127] M.-R. Gao, J.-X. Liang, Y.-R. Zheng, Y.-F. Xu, J. Jiang, Q. Gao, J. Li, S.-H. Yu, Nat. Commun. 6 (2015) 5982.

[128] X. Zhou, Y. Liu, H. Ju, B. Pan, J. Zhu, T. Ding, C. Wang, Q. Yang, Chem. Mater. 28 (2016) 1838–1846.

[129] M. Li, D. Wang, J. Li, Z. Pan, H. Ma, Y. Jiang, Z. Tian, RSC Adv. 6 (2016) 71534–71542.

[130] B.J. Inkson, Scanning electron microscopy (SEM) and transmission electron microscopy (TEM) for materials characterization, in: Mater. Charact. Using Nondestruct. Eval. Methods, Elsevier, 2016: pp. 17–43.

[131] U. Sikander, M.F. Samsudin, S. Sufian, K. KuShaari, C.F. Kait, S.R. Naqvi, W.-H. Chen, Int. J. Hydrogen Energy. 44 (2019) 14424–14433.

[132] M. Li, X. Wang, S. Li, S. Wang, X. Ma, Int. J. Hydrogen Energy. 35 (2010) 6699–6708.

[133] F. Wang, T. Wang, S. Sun, Y. Xu, R. Yu, H. Li, Sci. Rep. 8 (2018) 1–10.

[134] I. Zafiropoulou, M.S. Katsiotis, N. Boukos, M.A. Karakassides, S. Stephen, V. Tzitzios, M. Fardis, R. V Vladea, S.M. Alhassan, G. Papavassiliou, J. Phys. Chem. C. 117 (2013) 10135–10142.

[135] X. Zhao, H. Zhu, X. Yang, Nanoscale. 6 (2014) 10680–10685.

[136] Y. Li, L. Wang, S. Zhang, X. Dong, Y. Song, T. Cai, Y. Liu, Catal. Sci. \& Technol. 7 (2017) 718–724.

[137] C.F. Holder, R.E. Schaak, ACS Nano. 13 (2019) 7359–7365.

[138] S. Wang, D. Zhang, B. Li, C. Zhang, Z. Du, H. Yin, X. Bi, S. Yang, Adv. Energy Mater. 8 (2018) 1801345.

[139] K.-J. Huang, L. Wang, Y.-J. Liu, H.-B. Wang, Y.-M. Liu, L.-L. Wang, Electrochim. Acta. 109 (2013) 587–594.

[140] Z. Tong, Q. Ma, Y. Ni, T. Mei, J. Li, G. Dong, J. Mater. Sci. 54 (2019) 14354–14366.

[141] U. Sikander, S. Sufian, M.A. Salam, others, Procedia Eng. 148 (2016) 261–267.

[142] M. Chatti, T. Gengenbach, R. King, L. Spiccia, A.N. Simonov, Chem. Mater. 29 (2017) 3092–3099.

[143] A.B. Laursen, S. Kegnæs, S. Dahl, I. Chorkendorff, Energy \& Environ. Sci. 5 (2012) 5577–5591.

[144] J.G.N. Thomas, Trans. Faraday Soc. 57 (1961) 1603–1611.

[145] C. Hu, L. Zhang, J. Gong, Energy Environ. Sci. 12 (2019) 2620–2645.

[146] L. Yang, W. Zhou, J. Lu, D. Hou, Y. Ke, G. Li, Z. Tang, X. Kang, S. Chen, Nano Energy. 22 (2016) 490–498.

[147] A. Pandey, A. Mukherjee, S. Chakrabarty, D. Chanda, S. Basu, ACS Appl. Mater. \& Interfaces. 11 (2019) 42094–42103.

[148] T. Shinagawa, A.T. Garcia-Esparza, K. Takanabe, Sci. Rep. 5 (2015) 13801.

[149] Z. Lu, W. Xu, W. Zhu, Q. Yang, X. Lei, J. Liu, Y. Li, X. Sun, X. Duan, Chem.

Commun. 50 (2014) 6479–6482.

[150] X. Song, Q. Qi, T. Zhang, C. Wang, Sensors Actuators B Chem. 138 (2009) 368–373.

[151] M. Su, J. Wang, Sens. Lett. 9 (2011) 670–674.

[152] K.I. Han, S. Du Kim, W.S. Yang, H.S. Kim, M. Shin, J.P. Kim, I.G. Lee, B.J. Cho, W.S. Hwang, AIP Adv. 6 (2016) 35203.

[153] D. Zhang, J. Liu, B. Xia, IEEE Electron Device Lett. 37 (2016) 916–919.

[154] B. Hirschorn, M.E. Orazem, B. Tribollet, V. Vivier, I. Frateur, M. Musiani, J. Electrochem. Soc. 157 (2010) C452.

[155] D. Zhang, J. Tong, B. Xia, Q. Xue, Sensors Actuators B Chem. 203 (2014) 263–270.

[156] D. Zhang, X. Zong, Z. Wu, Y. Zhang, Sensors Actuators B Chem. 266 (2018) 52–62.

[157] L. Lai, L. Wang, H. Yang, N.G. Sahoo, Q.X. Tam, J. Liu, C.K. Poh, S.H. Lim, Z. Shen, J. Lin, Nano Energy. 1 (2012) 723–731.

[158] Q. Ke, M. Zheng, H. Liu, C. Guan, L. Mao, J. Wang, Sci. Rep. 5 (2015) 1–11.

[159] K. Jiang, T. Fei, T. Zhang, RSC Adv. 4 (2014) 28451–28455.

[160] T.C. Girija, M. V Sangaranarayanan, J. Power Sources. 156 (2006) 705–711.

[161] C. Portet, P.L. Taberna, P. Simon, C. Laberty-Robert, Electrochim. Acta. 49 (2004) 905–912.

[162] Y. Zhang, T. He, G. Liu, L. Zu, J. Yang, Nanoscale. 9 (2017) 10059–10066.

[163] J. Liu, J. Wang, C. Xu, H. Jiang, C. Li, L. Zhang, J. Lin, Z.X. Shen, Adv. Sci. 5 (2018) 1700322.

[164] Y. Gogotsi, R.M. Penner, ACS Nano. 12 (2018) 2081–2083.

[165] E. Senokos, V. Reguero, J. Palma, J.J. Vilatela, R. Marcilla, Nanoscale. 8 (2016) 3620–3628.

[166] X. Yang, C. Cheng, Y. Wang, L. Qiu, D. Li, Science (80-.). 341 (2013) 534–

537.

[167] J.R. Miller, R.A. Outlaw, B.C. Holloway, Science (80-.). 329 (2010) 1637–1639.

[168] A.B. Fuertes, M. Sevilla, ChemSusChem. 8 (2015) 1049–1057.

[169] E. Raymundo-Pinero, K. Kierzek, J. Machnikowski, F. Béguin, Carbon N. Y. 44 (2006) 2498–2507.

[170] J.B. Cook, H.-S. Kim, T.C. Lin, C.-H. Lai, B. Dunn, S.H. Tolbert, Adv. Energy Mater. 7 (2017) 1601283.

[171] X. Cong, C. Cheng, Y. Liao, Y. Ye, C. Dong, H. Sun, X. Ji, W. Zhang, P. Fang, L. Miao, others, J. Phys. Chem. C. 119 (2015) 20864–20870.

[172] B. Zhang, X. Ji, K. Xu, C. Chen, X. Xiong, J. Xiong, Y. Yao, L. Miao, J. Jiang, Electrochim. Acta. 217 (2016) 1–8.

[173] X. Liang, M. Chen, H. Zhu, H. Zhu, X. Cui, J. Yan, Q. Chen, X. Xia, Q. Liu, J. Mater. Chem. A. 8 (2020) 9068–9076.

[174] H. Xia, Y.S. Meng, G. Yuan, C. Cui, L. Lu, Electrochem. Solid State Lett. 15 (2012) A60.

[175] V. Subramanian, S.C. Hall, P.H. Smith, B. Rambabu, Solid State Ionics. 175 (2004) 511–515.

[176] H. Jiang, C. Li, T. Sun, J. Ma, Nanoscale. 4 (2012) 807–812.

[177] H. Jiang, T. Sun, C. Li, J. Ma, J. Mater. Chem. 22 (2012) 2751–2756.

[178] H. Zhao, H. Zeng, Y. Wu, S. Zhang, B. Li, Y. Huang, J. Mater. Chem. A. 3 (2015) 10466–10470.

[179] M. Kim, Y.K. Kim, J. Kim, S. Cho, G. Lee, J. Jang, RSC Adv. 6 (2016) 27460–27465.

[180] R. Khan, M.T. Mehran, M.M. Baig, B. Sarfraz, S.R. Naqvi, M.B.K. Niazi, M.Z. Khan, A.H. Khoja, Fuel. 285 (2020) 119174.